The Pennsylvania State University

The Graduate School

Department of Electrical Engineering

REMOTE SENSING TECHNIQUES IN THE INFRARED REGION OF THE ELECTROMAGNETIC SPECTRUM

A Paper in

Electrical Engineering

By

David M. Brown

Submitted in Partial Fulfillment
of the Requirements
for the Degree of

Master of Science
May 2005

The paper of David Michael Brown has been reviewed and approved by the following:

Date of Signature

_____ _____

C. Russell Philbrick
Professor of Electrical Engineering
Paper Adviser

_____ _____

Zhiwen Liu
Assistant Professor of Electrical Engineering

_____ _____

Kenneth Jenkins
Professor of Electrical Engineering
Head of the Department of Electrical Engineering

Acknowledgements

Everyone journeys to college for different reasons. I came to Penn State University 6 years ago thinking I knew what to do – thinking I wanted to be an engineering student. It took me until my senior undergraduate year to truly understand what that meant, and what the satisfaction of true engineering accomplishment felt like.

Throughout my time in graduate school for my masters degree, I owe many thanks to my advisor, Dr. Philbrick, as he was always full of excellent advice and guidance regardless of the situation. His constant challenges made the material in a class or research setting just difficult enough that struggling through to the solution provided for my acquisition of priceless skills in problem solving and reason. The "curious observer" approach taught by Dr. Philbrick was very supportive to my studies, as it opened my mind and allowed me to constantly fulfill the desire to ask the question, "why?" I also must mention my admiration for Dr. Liu's meticulous detail to thinking, helping and teaching. His lessons and suggestions will never be forgotten, and I owe many thanks to him as well.

I thank all of the supporters to my masters research outside of academia, primarily the ones from ITT Space Systems in Rochester, NY. I appreciate their willingness to authorize my continued participation on the ANGEL project. Constant involvement with the program made it possible for me to integrate much of my knowledge acquired in the classroom to real world applications.

My peers. How could I ever repay you? Without teamwork and the ability to bounce ideas around, my experiences in graduate school would never be as beneficial as they are. Joe, Adam, Sachin, and of course all my friends from undergrad, thank you all.

Lastly, but certainly not least, I thank my family; my father, my mother, my stepfather, and my sister. You all have stood right by my side for all these years and been there for me the instant you ever saw me start to think about stumbling. Thank you.

When the trials of life are upon me, or I feel that hope is fading, I think back to an email I received from Dr. Aydin when I was admitted to graduate school here at Penn State. When I look back I realize that I am truly am living proof that no matter what happens, it is never too late to turn things around. In the end, "hard work and commitment does lead to good things." – K. Aydin, Fri, May 16, 2003

Remote Sensing Techniques in the Infrared Region of the Electromagnetic Spectrum

Abstract

This study presents an overall review of remote sensing in the infrared region of the electromagnetic spectrum including explanations of how infrared radiative energy is created, emitted, and detected. Examples of infrared sources and detectors are presented with a detailed design example of how a scanning infrared camera can be used for midwave infrared measurements. Further, the study reviews how controlled emission and measurement of infrared energy can be used for Light Detecting And Ranging (LIDAR) applications. A modification of the Penn State DIfferential Absorption Lidar (DIAL) model was used in this study in an attempt to simulate the effects on performance due to transmitting beam misalignment – an important factor when implementing DIAL lidar theory into a commercial system. Simulation findings were closely reviewed for validity and subsequently compared to data acquired by the DIAL lidar used in the ITT Space Systems Airborne Natural Gas Emission Lidar (ANGEL) service. Significant correlation between the simulation results and data measurements were found by the study and thus provide validation that can be used for future performance estimates, or for troubleshooting applications.

Table of Contents

Introduction

Remote sensing using lasers has been shown to be the premier method to determine characteristics about the Earths environment over the last couple decades. With any active remote sensing technique, the wavelength of the active outgoing source is the limiting factor on how small a scattering entity can be characterized. Optical interaction with scattering entities in the far field became more widely known and accepted with the invention of the laser, a coherent optical source of electromagnetic radiation. The interaction of impinging electromagnetic radiation with a scattering entity results in either Mie particle scattering, Rayleigh molecular scattering, or Raman scattering, fluorescence, or absorption which is detectable at a remote location, typically close to the source of transmission [Philbrick 2003]. During fluorescence, the specific molecule is near electric state resonance, while for absorption the elections store resonant energy from the impinging energy source. One way of detecting these processes is most commonly referred to as LIght Detecting And Ranging, or LIDAR. Lidar techniques in the infrared utilize the spectral features for numerous molecules found in the region and as such can be used for a variety of applications.

Background in the Infrared

Spectral features found in the infrared are due to various modes of vibration, rotation, stretching, and bending which the bonds of the molecules experience. Unlike rotational spectra where the molecule of interest must have an inherent dipole moment, vibrational spectra arises when a changing dipole moment in the molecule is created due an asymmetrical stretch or vibration. The gross selection rule as outline by [Atkins, 1990] for infrared activity are that these vibrational motions must correspond to a normal vibrational mode of the molecule, where a normal mode is defined as a synchronous motion of atoms or groups of atoms that may be excited without leading to any further excitation. Symmetrical molecular vibrations or "molecular breathing" will not create a changing dipole moment and are thus infrared inactive [Atkins, 1990]. For example, the symmetrical stretch of CO_2 will not create a dipole moment, while one of the asymmetrical stretchs will yield a measurable spectral component as shown in figure 1 below. On the contrary, water H_2O, will never experience a symmetrical stretch and thus all modes will be infrared active as shown by figure 2.

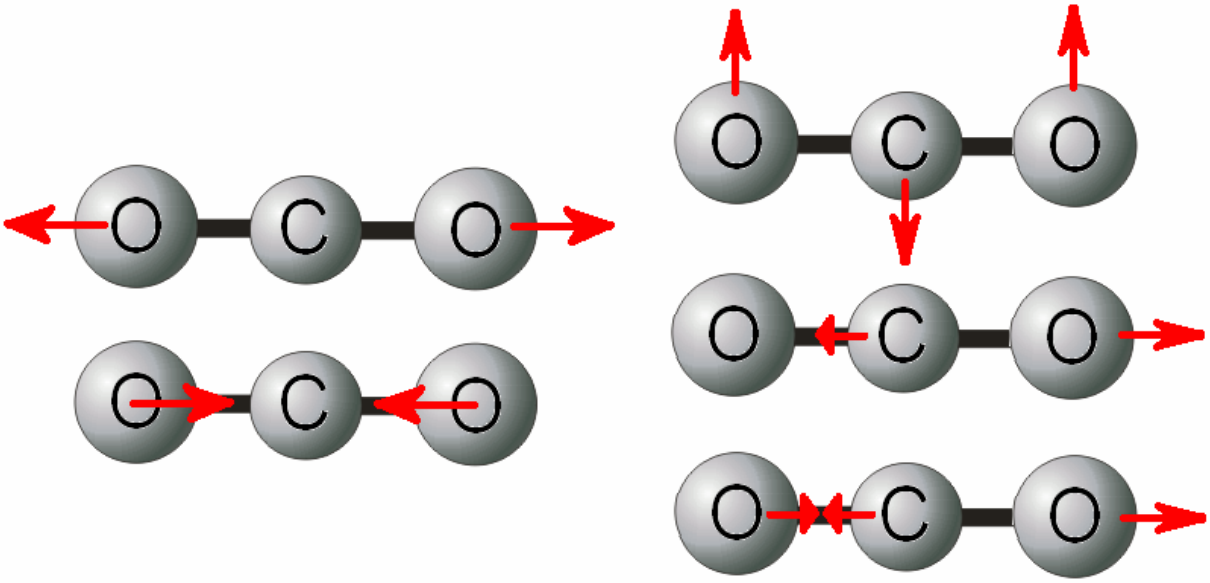

Figure 1: Asymmetrical and symmetrical stretches for CO_2, respectively [Atkins, 1990].

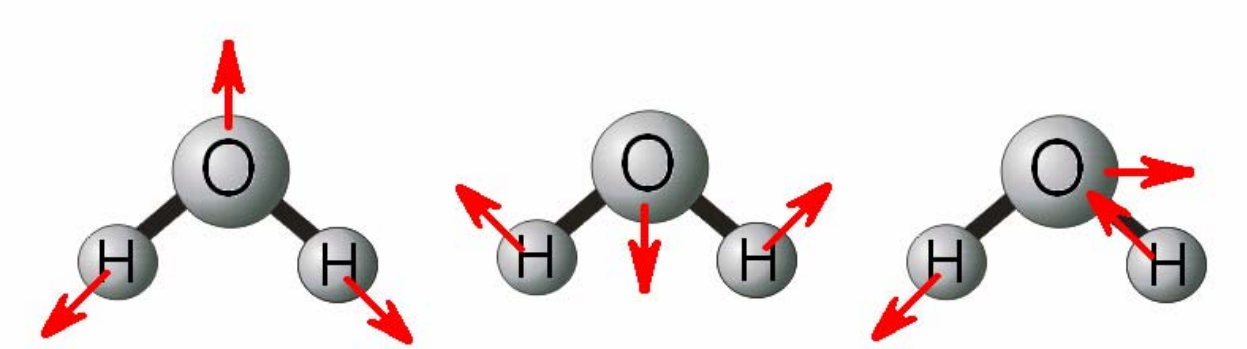

Figure 2: Possible stretching combinations for H_2O, all infrared active [Atkins, 1990].

Blackbody Emission

With a foundation in molecular physics, radiometry is the field that studies infrared emission to determine radiant infrared energy. Typically, measurements of radiant infrared energy are used for detecting temperature of remote objects, or describing temperature differences from a thermal background. In the most simple case, it is assumed that objects selected for measurement (humans, stoves, candles) are perfect blackbody radiators where the total isotropic radiated energy can be calculated by the following Stephan Boltzman law,

$$M = \sigma T^4, \qquad [1]$$

where,

M is the isotropic radiative emittance in watts per square meter [W/m^2],

σ is the Stephan Boltzman constant equal to 5.67E-8 $Wm^{-2}K^{-4}$, and

T is the temperature [K] [Wolfe 1996].

Isotropic radiators uniformly emit varying amounts of energy depending on wavelength as well as temperature. Figure 1 shows various Planck functions versus wavelength for different temperatures. The radiant exitance, M_λ in units [$W\ cm^{-2}\ \mu m^{-1}$], can be explained as the watts per unit area for a given wavelength interval. As the temperature of the blackbody radiator is

increased, the entire function will experience a blue shift, or an increase in the content of shorter wavelengths, while experiencing an increase in magnitude.

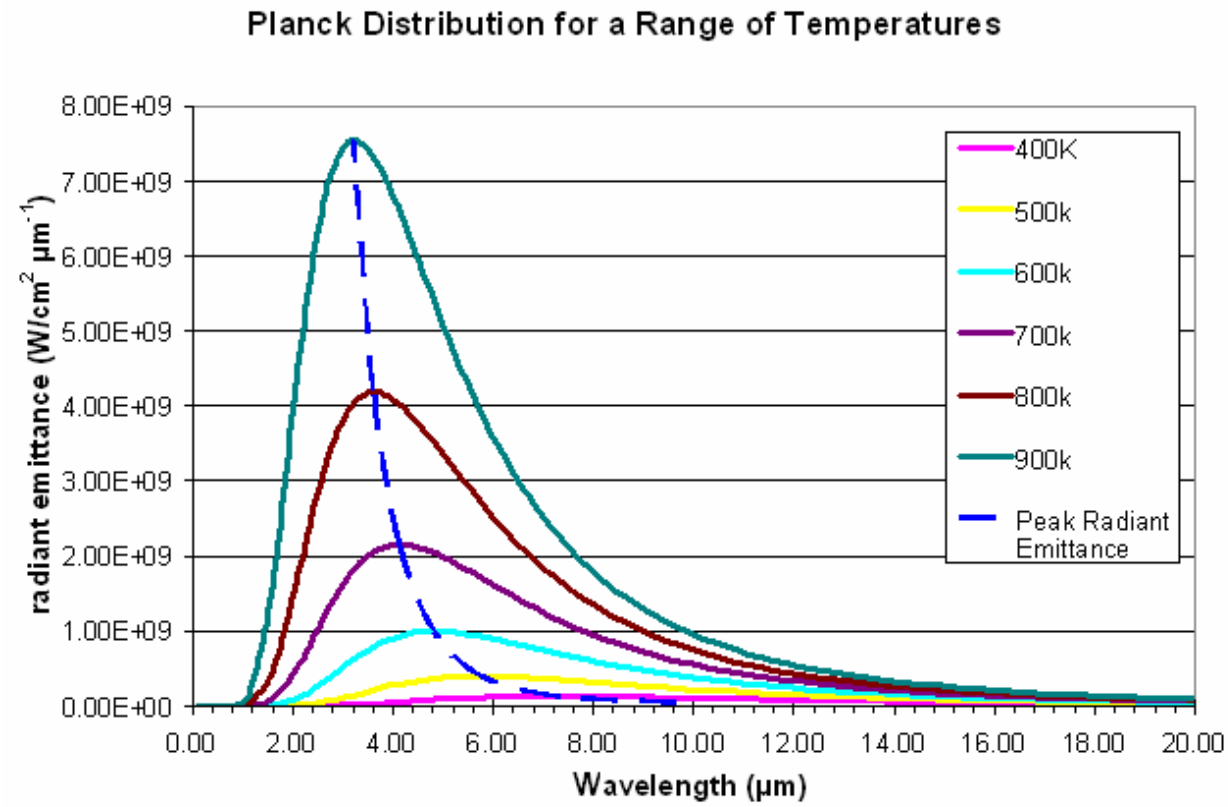

Figure 3: Planck functions for different temperatures show the change in peak radiant emittance.

Planck's Law describes the spectral distribution of radiation from a blackbody source with units of watts per square meter per wavelength interval as shown by

$$M_\lambda = \frac{2\pi c^2 h}{\lambda^5 \left(e^{\frac{hc}{\lambda kT}} - 1 \right)}, \qquad [2]$$

where,

c is the speed of light, 3E8 [m/s],

h is Planck's constant, 6.626E-34 [kg m^2/s]

k is Boltzmans constant, 1.38E-23 [J/K], and

M_λ is the radiant exitance emitted [$W/cm^2\ \mu m^{-1}$] [Wolfe, 1996].

The wavelength of peak radiative emission by a blackbody can be described by Wiens Displacement Law,

$$\lambda_{max} T = B\ , \qquad [3]$$

where,

λ_{max} is the wavelength of maximum radiative energy in meters [m],

B is the constant 2.898 X 10^{-3} meters-Kelvin [m K], and

T is the temperature in Kelvins [K] [Wolfe 1996].

Isotropic blackbody radiation is very helpful for characterizing detector systems, because the blackbody source exhibits a very broadband and continuous spectrum across a wide range of wavelengths. In addition, a simple increase in temperature provides for a easy way of increasing the intensity at a range of wavelengths.

Lambertian Surfaces

Infrared emission does not always occur in a purely spherical isotropic case, as if the radiation is due to a blackbody point source. Another important case, occurs when the emitter is a blackbody Lambertian surface or when the emission is a diffuse reflection of a collimated light source. In this case the source becomes the total radiative flux due to emission over 2π steradians instead of the full 4π steradians. The fundamental equation for radiation transfer can be used to calculate the differential element of power of two projected areas show by the following figure 4 and described by,

$$d\Phi = L\,\frac{dA_1\ cos\theta_1\ dA_2\ cos\theta_2}{R^2} \qquad [4]$$

where,

$d\Phi$	is the differential power element of two areas [W],
dA_1, and dA_2	are respectively the first and second projected areas [m^2],
θ_1, and θ_2	describe the orientation of the first and second projected areas,
R	is the distance between the two projected areas [m], and
L	is the radiance of the lambertian surface or the reflected radiance of the incident irradiance [W/m^2 sR] [Wolfe, 1996].

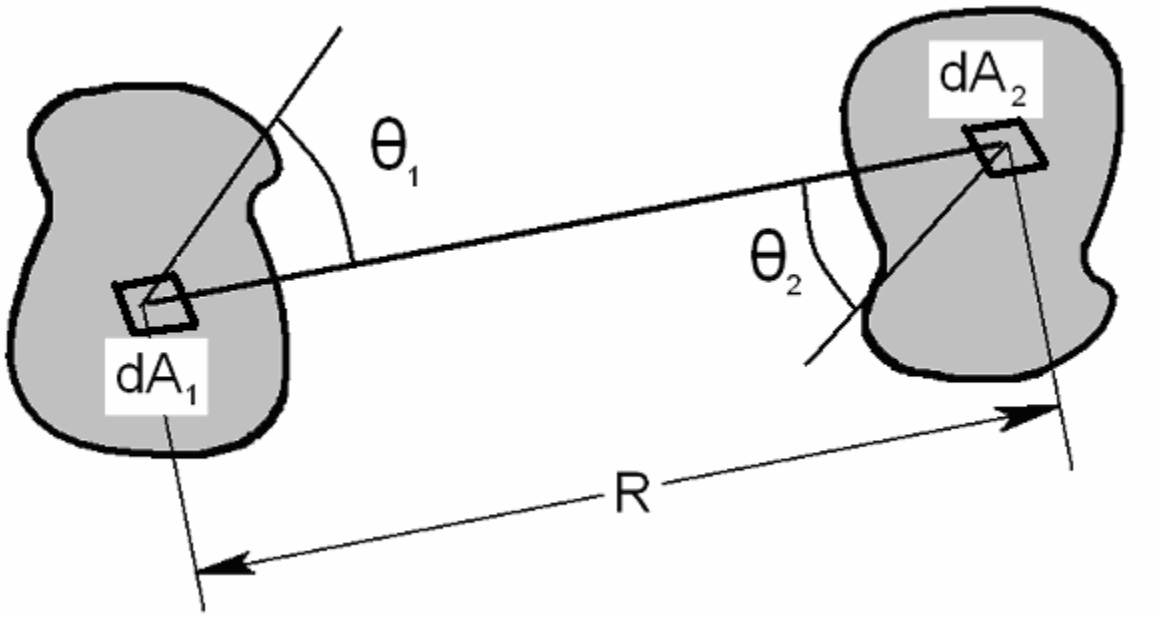

Figure 4: Fundamental equation for radiation transfer for two projected areas [Wolfe, 1996].

When one differential element is a Lambertian surface whether it be an emitter or a reflector, various simplifications can be made to equation [4] as the source is received by the second differential area as the first surface radiated over one hemisphere. Integration of this power over the entire emitting hemisphere, as shown by equation [5], will give the total emittance in watts per square meter of the Lambertian surface. This can subsequently be easily simplified to π multiplied by the radiance of the surface. [Wolfe 1996]

$$M = \frac{\int d\Phi}{dA} = \frac{P}{dA} = L \int_0^{2\pi} \int_0^{\pi/2} \sin\theta \cos\theta \, d\theta \, d\phi = L\pi \left[\sin^2\theta \right]_0^{\pi/2} = \pi L \,, \qquad [5]$$

where,

P is the total power emitted for one half of the total sphere [W], and

M is the radiant emittance [W/m^2].

In the case of a highly collimated light source impinging on a reflective surface of known reflectivity, the same logic can be applied to calculate the radiance given the incident irradiance intensity. This is possible only when it is assumed that the reflection is diffuse in nature and is shown by

$$L = \frac{I \, r_{dh}}{\pi} \,, \quad M = I \, r_{dh} \quad , \qquad [6]$$

where,

I is the incident irradiance in watts per square meter [W/m^2], and

r_{dh} is the reflectivity of the surface [unitless] [Wolfe, 1996].

Thus it is shown by equation [6], that the radiative emittance from a surface is equal to the reflectivity r_{dh} of the surface multiplied by the incident irradiance I. Noting that the units for radiative emittance, M and incident irradiance I are both watts per meter squared is consistent with these conclusions.

Measurement Techniques in the Infrared

Combining knowledge of blackbody radiators and Lambertian surface emission, it is possible to calculate the equivalent temperature of a perfect blackbody radiator required to match the reflected radiance of a monochromatic light source scattered from a diffuse reflecting surface. In theory, this is relatively easy by numerical methods. Knowing the wavelength of the impinging light would allow equation [2] to be solved numerically, and so determine the matching reflective radiance for an arbitrary temperature. If this calculation is performed, it can be shown that the temperature required to match the reflected radiance of a monochromatic source would be very low – significantly below room temperature. This would then in turn generate a Planck curve that would be out of detectable range and below the sensitivity threshold for most room temperature detectors. The alternative to this case is to use a notch filter in the detectable range of the detector in conjunction with an increased temperature.

Since any notch filter will have some amount of spectral width, the entire amount of radiation allowed to pass must be taken into account to arrive at the correct blackbody temperature value. In order to account for the emittance spread over a range of wavelengths, every wavelength interval that is allowed to pass must be multiplied by the percent transmittance of the filter function for the interval in question. Planck's Law can then be modified as follows to describe the observed radiative emittance seen through the filter given a temperature.

$$M = \sum_{\lambda_1}^{\lambda_1 + n(\Delta\lambda)} \frac{2\pi c^2 h}{\lambda^5 \left(e^{\frac{hc}{\lambda k T}} - 1 \right)} \Delta\lambda \, F(\lambda), \qquad [7]$$

where,

n is the number of wavelength increments [unitless],

$\Delta\lambda$ is the width of the wavelength interval in [m],

λ_1 is the beginning of the wavelength range of the filter [m],

M is the total radiant emittance seen through the filter [W/cm^2], and

$F(\lambda)$ is the transmittance for the notch filter at a given wavelength range +/- $\Delta\lambda/2$.

By performing the calculation for a range of temperatures and grayscale-matching the intensity of the calculated radiative emittance to an unknown radiative emittance from a diffuse source reflection, it becomes possible to arrive at a measured value of radiative emittance [W/cm^2].

The following simple calculation describes an example situation of how the radiant emittance would vary as a function of temperature through a notch filter. The fitting of a filter function by MATLAB for a standard notch filter centered at 3385nm commercially available through Nihon Dempa Kogyo Co., Ltd. (NDK) can be seen in Figure 5. Using equation [7] the radiative emittance passed through the filter as a function of blackbody temperature can be calculated as shown below in Figure 6.

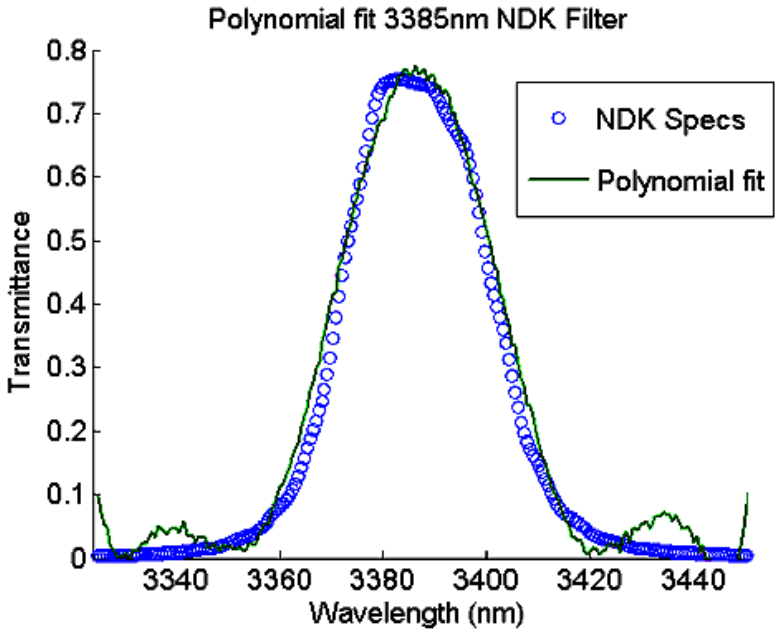

Figure 5: Transmission of 3385nm NDK filter fit compared with MATLAB polynomial fitting function.

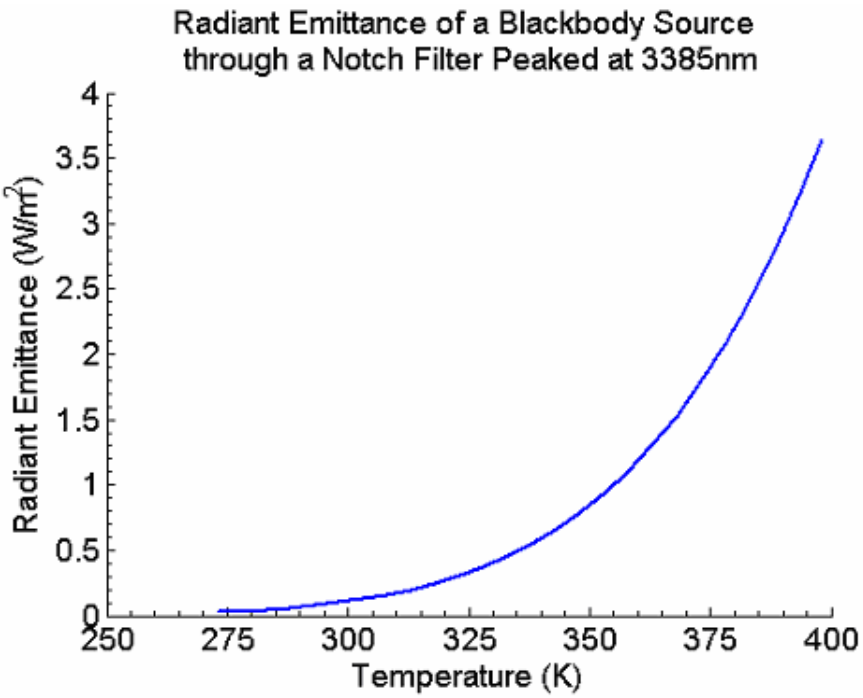

Figure 6: Emittance of a blackbody source observed through a NDK filter, as a function of temperature.

For this example calculation, it was assumed the radiant emittance per wavelength interval was constant over increments of one nanometer. Consequently, equation [2] was divided by 1000 to switch units into W/cm^2 nm before it was used in equation [7], where the numerator was multiplied by $1X10^{-9}$ corresponding to the averaging over one nanometer increments. The calculated equivalent blackbody temperatures as shown in Figure 3 are significantly above room temperature and therefore will create a signature that is above the noise floor of a detector. It should be noted that as the temperature of the blackbody source is increased, the plot tends to exhibit a linear dependence. This occurs because the tail of the Planck function although small in magnitude in comparison to the peak, grows in amplitude as it shifts to shorter wavelengths which can be seen in Figure 1. The shift at this point however is so drastic, that the tail section of the Planck curve in the wavelength range has a relatively constant slope for increased temperature values above 1000K (see Figure 7).

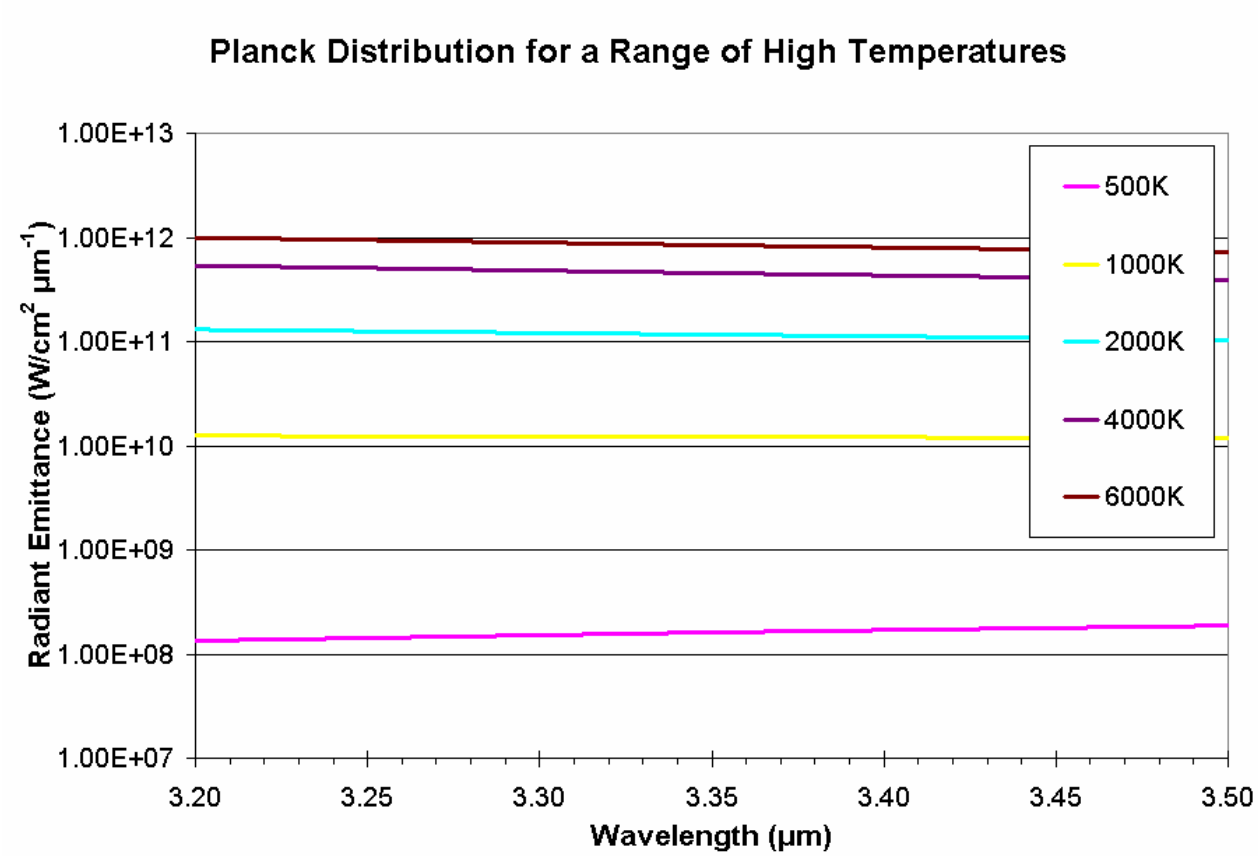

Figure 7: Planck distribution for a range of high temperatures in the 3.2 to 3.5μm midwave IR

It is the combination of large shifts in the Planck curves with respect to wavelength and DC offset increase in radiant emittance in this region that creates the linear effect at very high temperatures as seen in Figure 8.

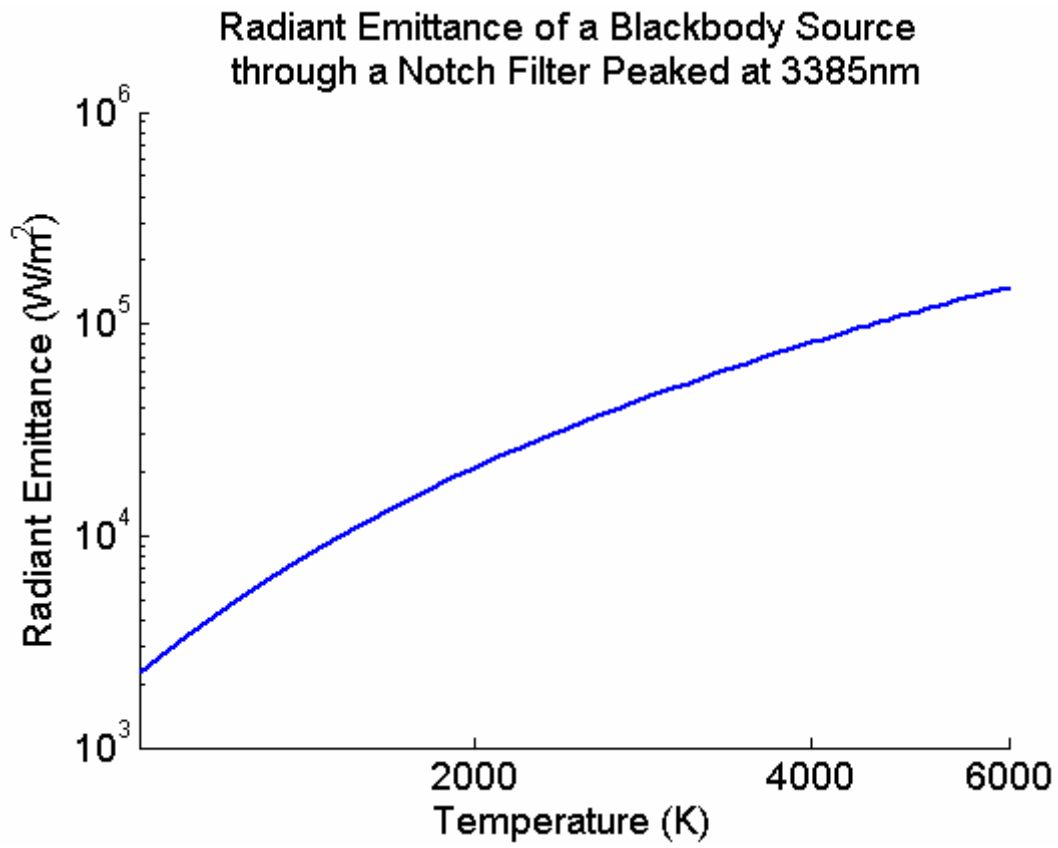

Figure 8: Emittance of a blackbody source observed through a NDK filter, as a function of high temperature.

In the experimental case, matching the intensity seen by a distant observer while recording blackbody temperature would allow the back calculation of the reflected radiance of a laser. Further, if the reflectivity of the target was known, the incident irradiance of the laser could easily be determined. This measurement case is limited to when the blackbody reference and the laser reflection are located at the same distance from the observer to keep the radiated energy per unit area as a constant in the comparison. Additionally, in the ideal case, the distant observers' measurement device would have a perfect notch filter allowing only the blackbody emission wavelength corresponding to the impinging laser to be passed and detected. Of course the narrower the notch on the filter, the higher the temperature of the blackbody source would need to be to generate the equivalent reflected radiance of the laser.

Infrared Hardware

There are many different types of hardware included in a review of such broad topics of infrared emitters, collectors, and detectors. IR sources can be classified into three categories; thermal sources, LED sources, and laser sources. Thermal heaters can be typically modeled as a blackbody source, with carefully designed blackbody sources following the model more closely. IR LED sources, like LEDs in other spectral regions, simply emit electromagnetic radiation at a specified infrared wavelength. The final type of infrared sources are infrared lasers. Lasers use the population inversion to cause stimulated emission of electromagnetic radiation at a desired wavelength, and of course have the advantages of narrow beams, narrow bandwidth and coherence. All three types of infrared sources can be operated in pulsed or continuous output configurations and each has its own share of applications.

All types of infrared detectors can be classified into one of two groups that describe their mechanism of transduction as being thermal or quantum. Thermal type infrared detectors fall into one of the following five categories: Thermopiles, Thermocouples, Bolometers, Pneumatic Detectors, and Pyroelectric Detectors [Wolfe, 1990]. All have individual characteristics, however they share the main feature of responsitivity with little dependence on wavelength. Thermopile infrared detectors use thermoelectromotive force between two conductors to create a detectable voltage; while bolometers are basically potentiometers that are sensitive to heat from infrared radiation. Pneumatic detectors use a material that produces a mechanical shift which can be measured by other methods when the device is subjected to infrared radiation. One type of pneumatic detector uses an infrared sensitive gas that expands when illuminated with infrared radiation to create the desired mechanical response [EO Industries, 2003]. Pyroelectric detectors

experience heating due to infrared radiation and thus produce a measurable electrical signal corresponding to a temperature variation.

The second main category of infrared detectors is typically denoted because quantum type infrared detectors. These detectors are very useful for remote sensing instruments as they have a very high detectivity and, a very fast response. Fast response is the quality that makes these types of detectors useful in a photon counting lidar applications. Their limitation is determined by photon noise. A major weakness to quantum type detectors is that they are more highly wavelength dependent than thermal detectors, and therefore usually require custom construction for a specific application. Photoconductive and photovoltaic infrared detectors fall into a sub category of quantum type IR detectors, which are solid state intrinsic detectors, and their performance is determined by their inherent energy gaps compared with the energy of wavelength to be measured. Photoconductive and photovoltaic infrared detectors, as their names suggest, change in conductivity and develop a varying voltage drop respectively when subjected to infrared radiation. Extrinsic type detectors are a final type of quantum detectors that are photoconductive detectors using doped germanium or silicon to control detector performance as a function of wavelength [EO Industries, 2003].

Examples of IR Field Measurements

Electromagnetic radiation in the infrared region of the spectrum can be viewed by integrating one or more infrared detectors into a camera platform. The Thermovision 400 Series IR Camera manufactured by Agema is one such apparatus capable of this type of measurement. An Agema 400 infrared camera was donated to Penn State University in the Spring of 2004 by a former PSU graduate and has been subsequently used to take infrared flux measurements of laser beams and blackbody sources. The Penn State Infrared Camera is a scanning type infrared

camera, meaning it uses high speed moving mirrors to scan through the field of the image while focusing on a single channel detector and updating a viewing screen. The following figure 9 shows the location of the numerous moveable mirrors and infrared focusing lenses.

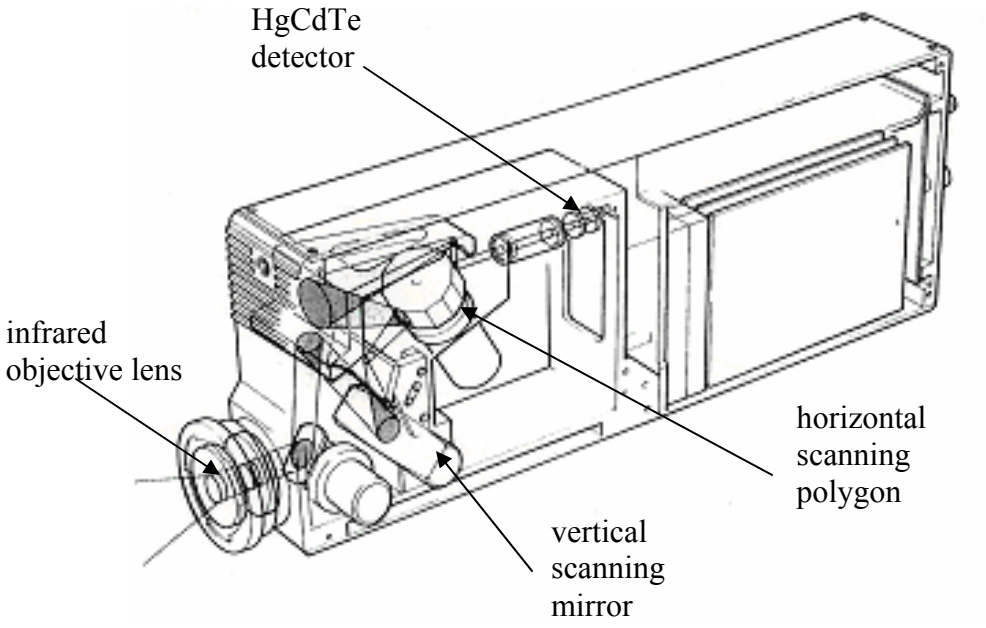

Figure 9: Parts of the Thermovision 400 Series Camera.

The main objective lens collects electromagnetic radiation in the 3-5um region of the spectrum, and focuses the energy on the first moveable mirror controlled by the stepper motor responsible for the vertical scanning of the camera's field of view. Following this, the infrared energy is reflected by three fixed mirrors onto a rotating mirror polygon which is responsible for the left to right scanning of the objective field of the camera onto the single mercury-cadmium-telluride (HgCdTe) detector. The synchronized movement of these two mirrors creates an infrared image with 100 element linewidth, a resolution of 140 visible lines, and updates 20 times per second.

The following Table 1 describes the complete specifications for Penn State University's Thermovision 400 Series IR Camera.

Table 1: Specifications of Thermovision 400 Series Camera

Specifications	
Spectral Range	2μm – 5μm
Imaging Type	Scanning/ single detector
Camera Resolution in pixels	140 X 100
Maximum Camera Refresh Rate	20 Hz
Dynamic Range	12 bit
Thermal Sensitivity	0.1°C
Data Acquisition Hardware	WinTV USB and Laptop with available USB port
Data/Image Acquisition Software	WinTV 2000, Virtualdub
Data Analysis Software	Matlab
Sampling Frequency	fixed by camera resolution and refresh rate
Data Format Types	Analog/Digital
Analog Connection (format)	BNC (RS-170)

The camera uses a quantum type HgCdTe photovoltaic detector that monitors the excess current carriers in the material generated by the impinging infrared electromagnetic radiation. When a small section on the active surface of the HgCdTe is excited by the infrared radiation, excess charge is generated in the region. As the focused image is scanned down the strip, additional charge is produced and carried with the initial free electrons. The arrival of this energy barrage at the end of the detector strip increases the signal to noise ratio by several orders of magnitude before any type of data processing.

When attempting to measure a pulsed source with the camera, the result was quite fascinating. Since the camera is a scanning type, every object within the field of view of the camera is independently scanned and subsequently imaged onto the image plane of the camera.

Consequently, a pulsed source that has a repetition rate that is on the order of the refresh rate for adjacent pixels will not be completely imaged. In the case we have examined, the camera and the laser both operate close to the same repetition frequency. It is thus shown that as the camera scans to the location of the next pixel, the laser distribution will no longer be active in the field of view of the camera. This effect when observed in the experimental case creates a pattern of nearly vertical lines which corresponded to the points in time when the spatial scanning of the camera sampled the backscattered power of a laser impinging on a target board. Figure 10 shows a series of snapshots taken by the camera under this case.

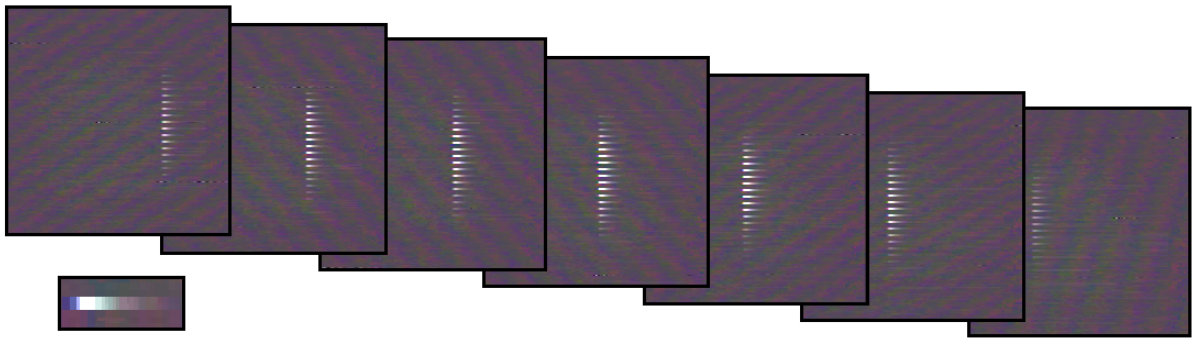

Figure 10: Series of snapshots taken by camera imaging reflection of pulsed laser distribution.

As is evident from the frames of data taken from the IR camera video, very little is observed about the laser distribution reflected from the target board from a single frame. In order to create a more detailed image, it becomes necessary to take an entire series of images and integrate them together. Since the repetition rate of the laser and the scanning frequency of the camera were fixed during the length of the data set, the spacing of the samples were also fixed. Using Matlab, an adaptive virtual grating was correlated with a single frame halfway through the movie taken with the IR camera which allowed the spatial calculation of every subsequent sample in the field of view. After the vertical spacing of the grating was known, the entire movie was processed to

determine the horizontal location of the point in each frame per signal line where a cross section in the far field was first sampled. The trail off of the signal as seen in Figure 10 was disregarded to avoid skewing the relative intensity readings of the laser distribution as the image was integrated. The complete resampled image was then smoothed to create the final outputs shown in Figure 11.

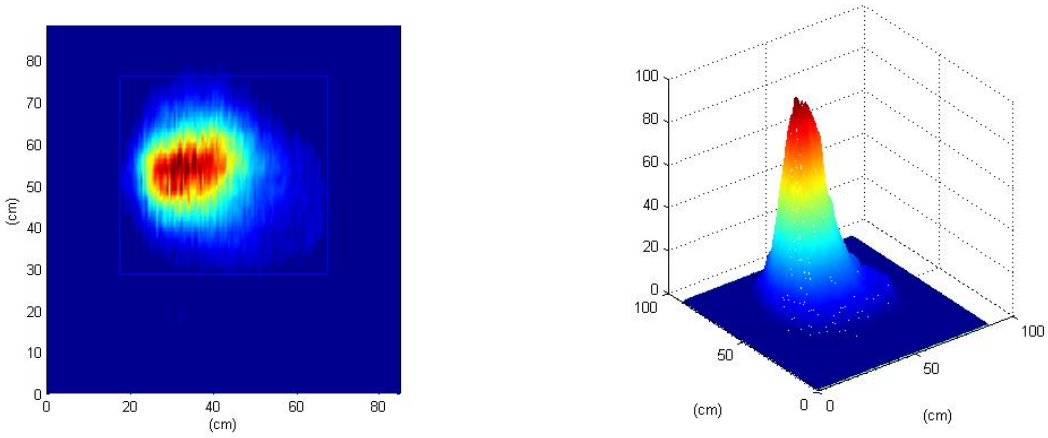

Figure 11: Integrated pictures of far field distribution of laser beam reflecting off diffuse surface.

One defining characteristic of every data set taken of a pulsed source by the camera are the length trails as shown in Figure 10. It has been concluded after reviewing many instances of data collected by the IR camera that the lengths of these trails are directly proportional to the length in time, intensity, and repetition rate of the pulse impinging on the target board that one should expect.

Remote Sensing in the Infrared

Understanding the influence of atmospheric, angular, and topographic effects in the infrared region of the electromagnetic spectrum is what allows us to track the loss terms through a remote sensing system. A large advantage to remote sensing in the 3-5μm region of the IR is that the Earth's atmosphere has a relatively low background radiance in this midwave infrared region of the electromagnetic spectrum. The sun viewed as a typical blackbody source has a peak of radiation at 500 nm in the spectrum and severely interferes with any active remote sensing measurements in the visible spectrum. Although the Earth itself has its own background radiance that peaks at about 10 μm in the infrared, the signature at 3-5μm is orders of magnitude below that of the visible spectrum intensity. This lends well to low power active remote sensing in the region, with the optimal location for operation being where the combined effects of the Earth-Sun background radiance falls to a minimum in the 3-4 μm range. Figure 12 was calculated using MODTRAN for the case of an observer looking down at the surface of the Earth from an altitude of 100km. The plot shows the average radiance as a function of wavelength for the summer of a mid latitude location.

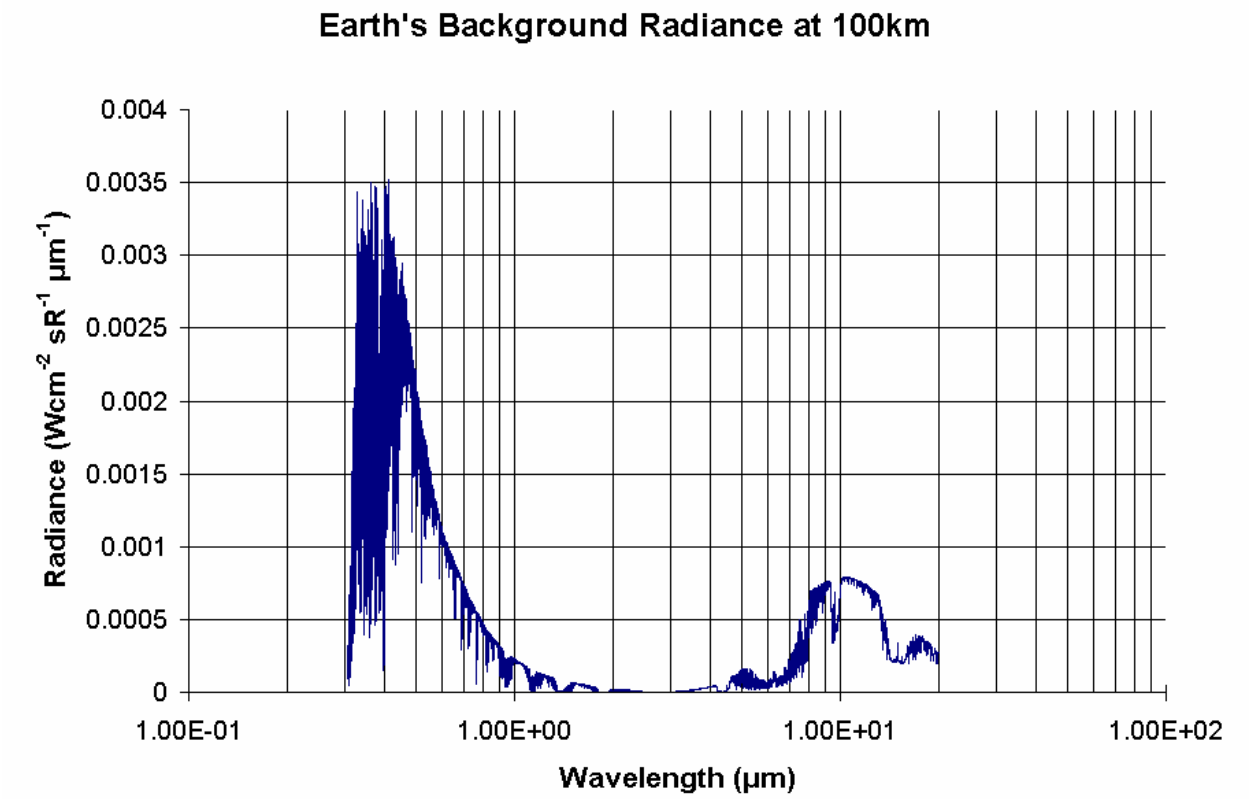

Figure 12: MODTRAN simulation of Earth's background radiance at 100km.

Performance of a remote sensing system taking advantage of the 3-4 µm range of the spectrum is relatively constant independent of the time of day as the Sun's effect is minimal. Any of the lidar techniques outlined [Philbrick 2003] can be implemented in this region of the spectrum with enhanced signal to noise ratio due to this low background. The following discussion will focus on the explanation of the DIAL method, along with the explanation of models created to simulate performance. Calculations compared with an example DIAL system operating in the 3-4 µm range are described.

The DIAL Method

The DIAL (DIfferential Absorption Lidar) method utilizes two laser wavelengths, one on the absorption feature of a given molecular species and one slightly off this absorption feature. Upon transmission of these two wavelengths, the laser tuned to the absorption feature of a given species is attenuated in proportion to the number of molecules of the absorbing species. The signal ratio to the off-line can be used to quantify the amount of the substance on the path. The change in fraction of the returning energy scattered back from each interval that arrives back at the transmitted location of a monostatic system from the elastic scattering of atmospheric aerosols and particulates characterize the profile of the species. The Differential Absorption and Scattering method (DAS) uses a hard target to return to measure the path integrated species concentration using the signal's scattered energy back to the receiving lidar telescope [Measures 1984]. Long Path Absorption (LPA) is another term for DAS, and it places a less stringent requirement on transmitted power, because a topographical target typically returns 10^3 to 10^9 more energy to the detector than DIAL profiles obtained from atmospheric scattering. When a high sensitivity measurement is required, LPA is the preferred method; however range resolution and knowledge of target scattering properties are compromised because the scattering entity is usually at a fixed range from the origin of the transmitted energy pulse [Measures 1984]. This technique is often used to observe a plume that only exists over a small range in the laser path. The following derivation describes the characteristics of a long path absorption system. The derivation of number density for both of the DIAL cases stems from the basic lidar equation for returned power due to elastic scattering is presented by [Measures 1984] as,

$$P_{rec}(\lambda, R) = P_{out} \frac{A}{R^2} \frac{c\tau_L}{2} \xi(\lambda)\xi(R)\beta(\lambda, R) e^{-\int_0^R \kappa_T(R)dR}, \qquad [8]$$

where,

P_{out}, P_{rec}	are the respective powers [J] transmitted and received per pulse at wavelength λ,
A	is the area of the receiving telescope [m^2],
c	is the speed of light [m/s],
τ_L	is the pulse duration period [s],
R	is the range to the scattering entity [m],
$\xi(\lambda)$	is the total optical efficiency at wavelength λ for all optical elements [unitless],
$\xi(R)$	is the probability that radiation from range R reaches the detector based on geometrical considerations,
$\beta(\lambda,R)$	is the backscatter cross section [m^{-1}] of the volume element for the laser wavelength λ
$\kappa_T(R)$	is the total attenuation coefficient at wavelength λ at range R [m^{-1}].

Because we are attempting to characterize a differential absorption system, it becomes necessary to expand on the basic lidar equation to compare the energy returned by two different laser transmissions. The return energy for a pulse transmitted on and slightly off the absorption feature of a species of interest can be described via the equations derived from elastic scattering equation [8],

$$E_{rec,on}(\lambda_{on}, R_T) = E_{out,on} \frac{A}{R_T^{\,2}} \xi(\lambda_{on}) \xi(R_T) \frac{\rho^s \tau_d}{\pi \tau_L} e^{-2 \int_0^{R_T} \left[\kappa(\lambda_{on},R) + N(R)\sigma^A(\lambda_{on})\right] dR}, \qquad [9]$$

$$E_{rec,off}(\lambda_{off}, R_T) = E_{out,on} \frac{A}{R_T^{\,2}} \xi(\lambda_{off}) \xi(R_T) \frac{\rho^s \tau_d}{\pi \tau_L} e^{-2 \int_0^{R_T} \left[\kappa(\lambda_{off},R) + N(R)\sigma^A(\lambda_{off})\right] dR}, \qquad [10]$$

where,

$E_{out,on}$, $E_{rec,on}$	are the respective energies transmitted and received per pulse at the on or measurement wavelength [J],

$E_{out,off}$, $E_{rec,off}$	are the respective energies transmitted and received per pulse at the off or reference wavelength [J],
R_T	is the range to the topographical scattering target [m],
$\xi(\lambda_{on})$ $\xi(\lambda_{off})$	are respectively the total optical efficiency at on and off wavelengths λ_{on} and λ_{off}, for all optical elements [unitless],
$\xi(R_T)$	is the probability that radiation from range R_T reaches the detector based on geometrical considerations,
τ_d	is the detector integration period [s],
τ_L	is the pulse duration period [s],
ρ^s	is the scattering efficiency[unitless],
$\sigma^A(\lambda_{on})$, $\sigma^A(\lambda_{off})$	are the respective absorption cross sections[m^2] for the species of interest at the online and offline wavelengths λ_{on} and λ_{off},
$\kappa(\lambda_{on},R_T)$, $\kappa(\lambda_{off},R_T)$	are the respective attenuation coefficients of the atmosphere to the online and offline wavelengths λ_{on} and λ_{off} independent of the absorbing species,
N(R)	is the number density of the absorbing species[# m^{-1}] and,
A	is the area of the receiving telescope [m^2].

Notice that backscatter term has been replaced with the scattering efficiency of the target and that there is an additional factor of π present on the denominator of the equation. Recalling our earlier argument stating that laser reflections off a target create a diffuse reflection allows for the justification of this extra term assuming it is modeled as a Lambertian emitter. The ratio of the detector integration time to the pulse integration time is placed in the equation in an event that the pulse length is longer than the integration time of the detector. This would conclude that the detector would not be observing the total attenuation by the species of interest and consequently skew the total concentration measurements for the path of propagation. Typically, the detector integration time is long enough to capture the entire return pulse, and when this is the case, the detector integration time to pulse length ratio can be set to unity [Measures 1984]. If a ratio

between the two total return energies is taken, many of the variables present in both equations can easily be canceled out assuming the transmitted wavelengths are spectrally close to each other and thus have the same fraction of scattered intensity from the target. Optical efficiency, and reflectivity can first be canceled out when the ratio is taken; consideration must be given to verify that the transmitted on and off wavelengths have approximately the same target reflectance. The transmitted energy by the measurement and reference lasers will typically create a constant out in front of the equation [11], which can be monitored assuming the energy for each laser is tracked during operation. As such, we can assume for the ideal case that these energies are equal and therefore can be canceled out of the ratio. If it is assumed that the lasers are similar in configuration and that both are transmitting on the same optical axis, the ratio of the offline return energy to the online return energy can be further simplified as,

$$\frac{E_{rec,off}(\lambda_{off},R_T)}{E_{rec,on}(\lambda_{on},R_T)} = e^{2\int_0^{R_T}[N(R)]dR\left[\sigma^A(\lambda_{on})-\sigma^A(\lambda_{off})\right]-\kappa(\lambda_{off},R)+\kappa(\lambda_{on},R)} \quad [11]$$

This ratio can then in turn be solved for the integrated concentration of the absorbing species along the path of propagation,

$$\int_0^{R_T} N(R)dR = \frac{1}{2\left[\sigma^A(\lambda_{on})-\sigma^A(\lambda_{off})\right]}\left[\ln\left[\frac{E_{rec,off}(\lambda_{off},R_T)}{E_{rec,on}(\lambda_{on},R_T)}\right]+\kappa(\lambda_{off},R)-\kappa(\lambda_{on},R)\right],$$

$$= \frac{1}{2\sigma^A_{diff}}\left[\ln\left[\frac{E_{rec,off}(\lambda_{off},R_T)}{E_{rec,on}(\lambda_{on},R_T)}\right]+\kappa(\lambda_{off},R)-\kappa(\lambda_{on},R)\right], \quad [12]$$

where,

$$\sigma^A_{diff} = \sigma^A(\lambda_{on})-\sigma^A(\lambda_{off}), \quad [13]$$

and is denoted as the differential absorption cross section[Measures 1984]. The differential absorption cross section is the fundamental reason as to why attenuation occurs for a concentration of gas being observed.

DIAL Error Sources

As shown, the atmospheric effects for the measurement and reference beams, $\kappa(\lambda_{on},R_T)$, $\kappa(\lambda_{off},R_T)$ are factors in the final equation for the selected species. These factors can be further described using an example DIAL lidar operated by Shell Research Ltd. and SESL in addition to other error sources. Shell Research Ltd. and SESL have together operated an infrared DIAL lidar to measure methane, ethane and heavier alkanes since 1995. It is capable of measuring hydrocarbon concentrations well below 1ppm at ranges up to about 1km, and is fixed in a standard shipping container [Walmsley, O'Connor 1997]. The lidar uses a DAS technique to acquire column concentration through elastic scattering off atmospheric aerosols and particulates. Although this approach slightly differs from our previous derivation of hard target return concentration path length measurements, both methods experience similar factors that influence the lower detectable limit of the system.

Walmsley and O'Connor outline six effects in the Shell, SESL system that can contribute to error in addition to detector noise. These sources of error can be defined as follows by,

(1) difference in backscatter coefficient as seen by the measurement and reference beams due to imperfect beam overlap and imhomogenities in the atmosphere,
(2) movement of the atmospheric inhomogenities between measurement and reference pulses,
(3) difference in optical efficiencies due to asymmetries of the transmitted beams or optical axes alignment with the reciever,

(4) differential attenuation of measurement and reference beams by scattering,
(5) constant variation in the backscatter coefficient due wavelength difference of measurement and reference beams, and
(6) temporal backscatter variations along the line of propagation [Walmsley, O'Connor 1997].

These sources of error give a good baseline as to account for the error experienced by either of the DAS or LPA DIAL methods discussed. The difference in backscatter coefficient as seen by the measurement and reference beams due to imperfect beam overlap is a major error source present in the design of both systems. Imperfect beam overlap in fact has a larger effect on LPA techniques as the topographical target of interest can vary in reflectivity more significantly than does molecular backscatter. Movement of atmospheric inhomogenities between the measurement and reference pulses would weakly affect the LPA technique, however a varying topographical target in the case of LPA would intensify the effect in the same manner. As such, very close spacing of the transmitted measurement and reference pulses must be established. In the event of a scanning system, rate of scan as compared to the time between pulses must be taken into account. The difference in optical efficiencies due to asymmetries or misalignments would be equally important in both cases. If we assume that the wavelengths used are relatively close to each other, the differential scattering and backscattering due to the wavelength difference is negligible.

The ANGEL System

ITT Industries owns a multi-wavelengths DIAL lidar operating in the infrared region that can rapidly and economically locate, identify, and quantitatively map hazardous chemical releases [Stearns, et. al, 2004]. The lidar was built by Coherent Technologies Inc. under contract

from Eastman Kodak Company and is capable of filling a broad range of chemical measurement needs due to tunabilty of the measurement and reference wavelengths between 3 and 5 μm. The system is installed on an airborne platform that provides a ground resolution better than 1 m at flight speeds in excess of 75 m/s for mapping surface-source chemical plumes [Grund, et.al., 2004]. The ITT Industries Airborne Natural Gas Emission Lidar (ANGEL) service uses the lidar to map both methane and ethane gas emissions due to leaks in natural gas pipelines, where the gas consists of about 96 % is methane, 3% is ethane and the remaining 1% various other components. Typically, the concentration of methane in a leak plume will add significantly to provide a signal that is well above the integrated background atmosphere levels [~1.7ppm X path length] and therefore is detectable through LPA DIAL methods. Background methane concentration levels can sometimes cause interference with measurements as the readings are sometimes due to livestock, sewage plants, etc instead of natural gas pipeline leaks. Although ethane levels in natural gas are much lower concentration, the presence of an ethane signature allows the system to confirm the natural gas leak detection, since the normal background level is small, and there are no other significant sources.

Detection of methane and ethane at range is possible by the infrared activity of these molecules. The important hydrogen bonds associated with CH asymmetrical stretching vibration in hydrocarbon species are responsible for the spectral features in the midwave infrared where the system operates as shown in Figure 13.

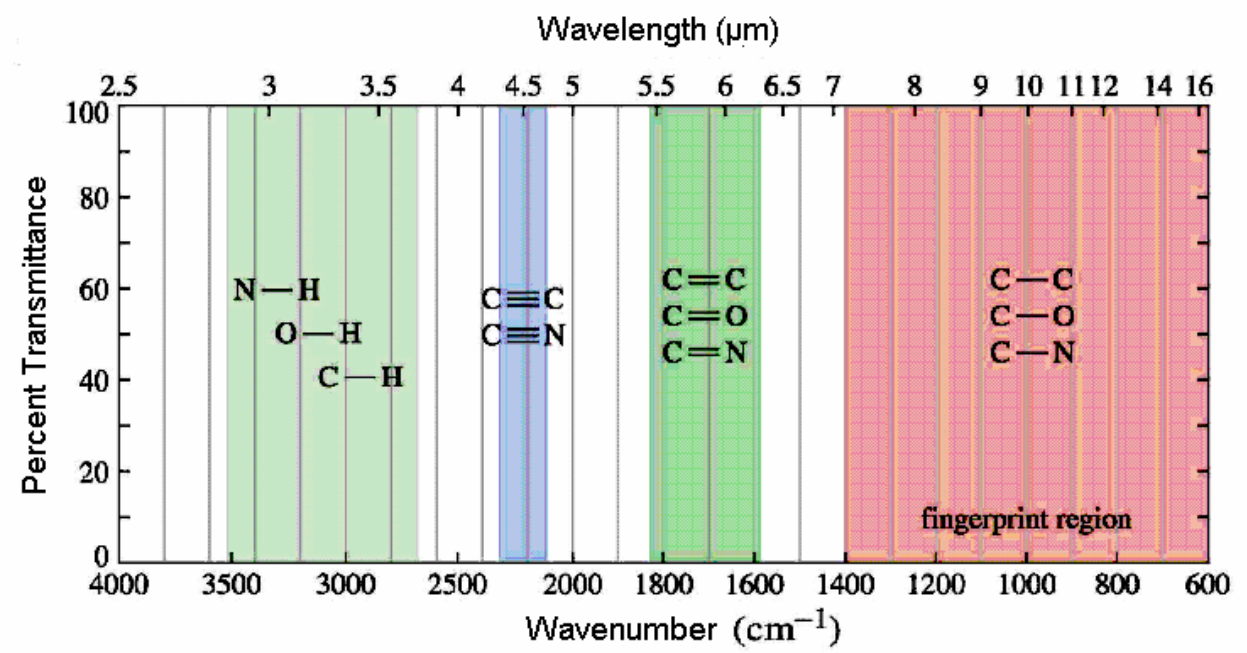

Figure 13: Radiation due to vibrational infrared emission of various typical bonding structures.

A simple numerical calculation assuming the force constant of carbon hydrogen bond is about 470 N·m allows us to calculate the angular frequency ω of $5.5X10^{14}$ rad/s assuming the reduced mass of a CH molecule $21.71X10^{-27}$ kg. This implies that the radiation lies around 3.4 μm which is within the operational region of the instrument. This same logic can be applied to methane, however there will be various emissions in the region of the spectrum due to several possible vibrational modes.

DIAL LIDAR Simulations

A simulation model for DIAL lidar measurements was created in order to investigate a combination of several of the previously described error sources that may occur during operation. The model (DIALSim) can be configured to model measurements taken by the DIAL lidar used in the ANGEL service offered by ITT Industries Space Systems division. While the details of this specific lidar and equivalent model parameters cannot be released at this time, the quantitative simulations described in this section use arbitrary parameters, and overall trends in the response of the system will be examined.

In order to make DIALSimV2 as complete as possible, various error sources derived from Walmsley and O'Connor's work were integrated into the model [Walmsley, O'Connor 1997]. One of the most frequently experienced error sources discussed was a case of beam misalignment in the far field relative to differences in topographic reflectance. DIALSimV2 allows the user to enter each beam's divergence and their center to center separation distance in addition to topographical reflectance values to model this error effect. Another frequently occurring error parameter outlined by the work of Walmsley and O'Connar was transmitter and receiver misalignment and the effect on the systems optical efficiency parameters. While the simulation does not allow for input of transmitter and receiver alignment, it does permit efficiencies for both the reference and measured pulses on the transmitting and receiving sides of the system to be entered.

Other error sources outlined by Walmsley and O'Connar can be justifiably excluded from the model due to the small magnitude of their effect upon the final concentration path length (CPL) estimates. It is assumed in the simulation that the transmitted online and offline pulses are spaced close enough in time that differential effects on their individual atmospheric propagation

or topographic reflection are not significant. Working under the assumption that the measurement and reference wavelengths are spectrally close in addition to being close in time allows us to consider the differential wavelength effects of backscatter, scatter, and topographic reflections to be negligible. Figure 14 shows the main DIALSimV2 Matlab GUI interface.

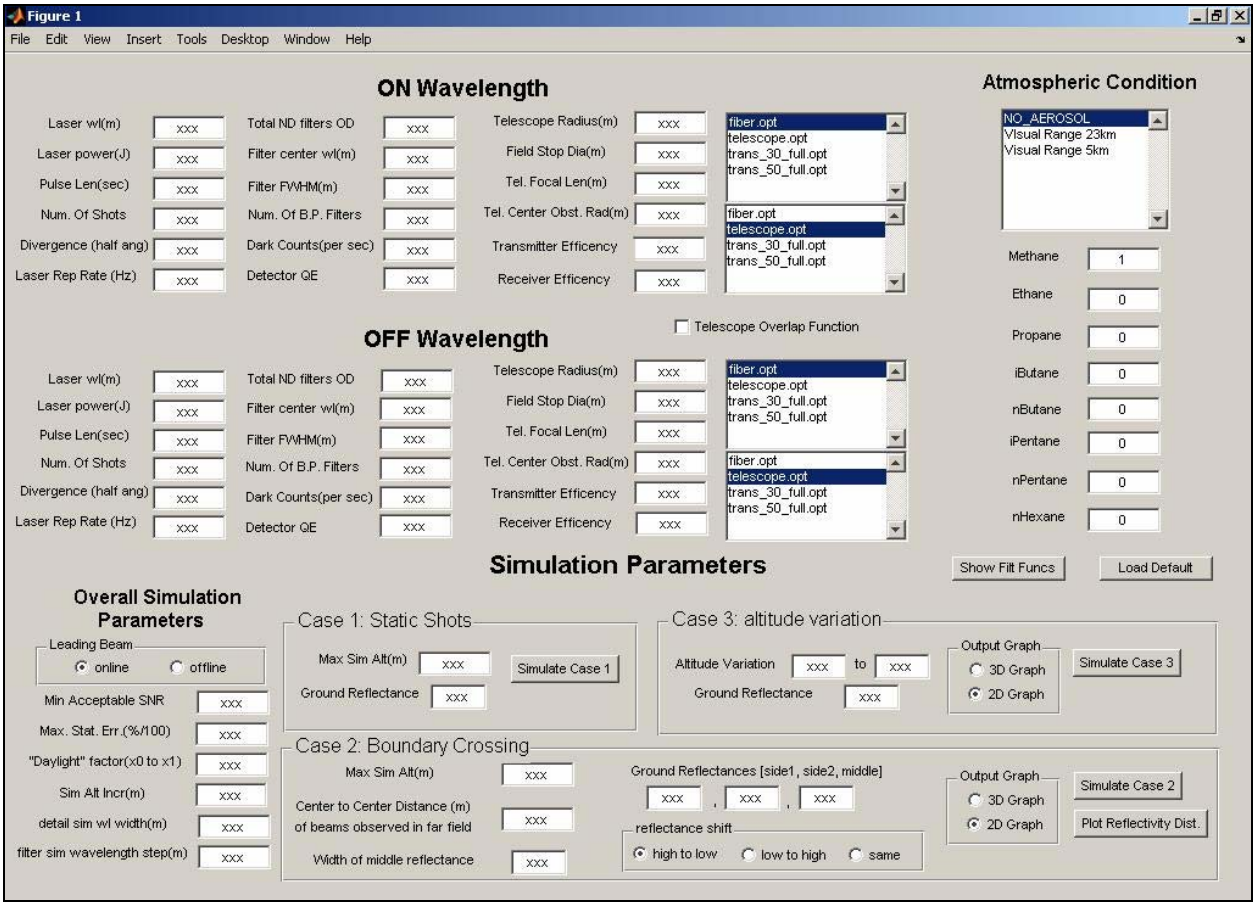

Figure 14: DIALSimV2 GUI Interface.

Example Simulations and Cases

The PSU DIAL model is currently configured to run for three separate cases. The original programs have evolved from the work of several graduate students, particularly the recent effors by Guangkun Li [Li, 2004] and it has since been modified to model additional conditions experienced in a real world type setting. The original program, DIALSimV1, was

used to describe expected signals returned for measurements of returned as ground level concentration by a single shot DIAL analysis system measureing gas plumes near the surface from an elevated platform. This model has been reworked into DIALSimV2 and is currently denoted as 'Case 1'. An example of a Case 1 simulation for arbitrary parameters is shown below in Figure 15.

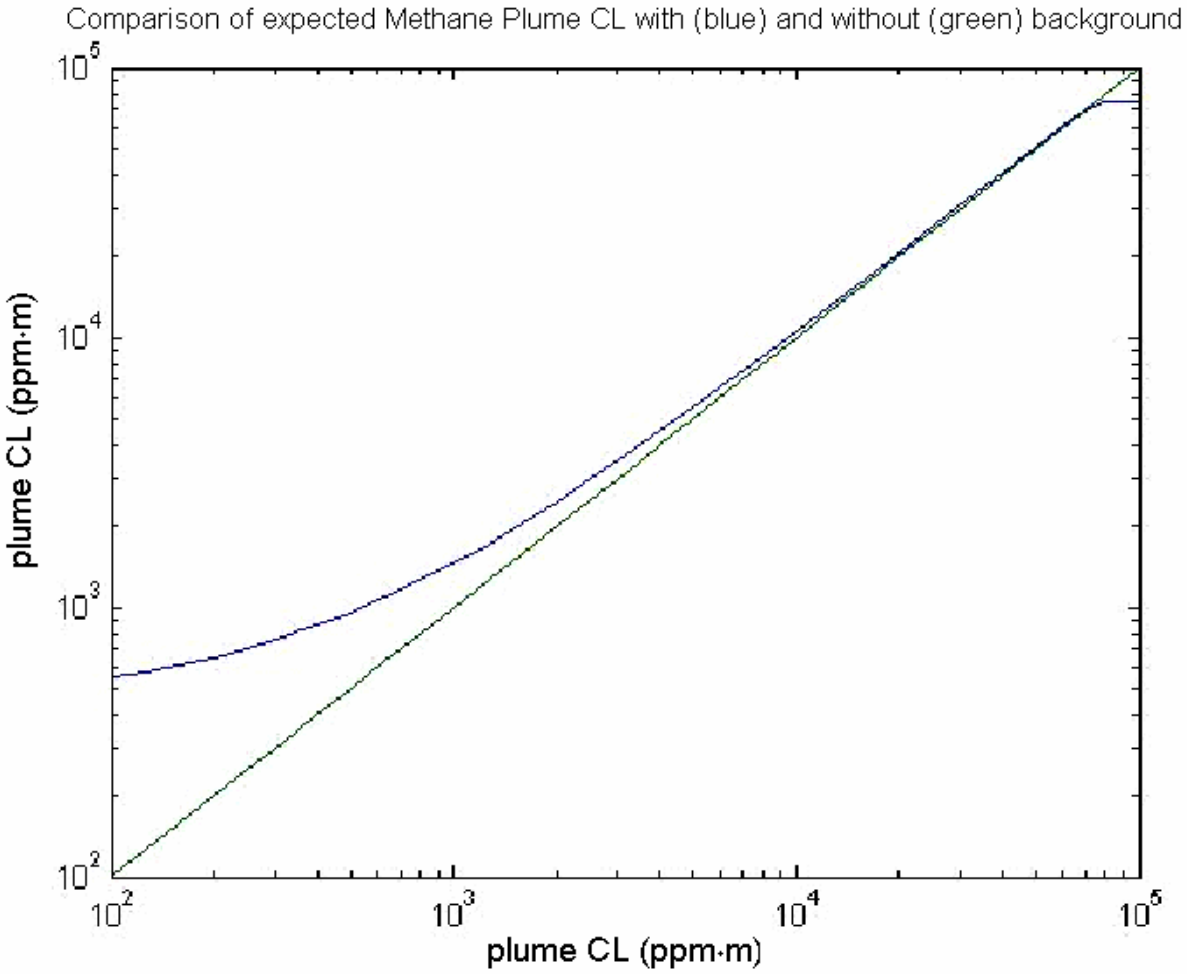

Figure 15: Path concentration as a function of leak size for an altitude of 500m.

As shown, the natural background methane causes the deviation from the idealized CPL measurement when imaging smaller plumes. At larger methane plume concentrations, the effect of the background is lessened as the signal to noise ratio .

'Case 2' permits the user to simulate a case when the measurement and reference beams not perfectly overlapped, and is used to study the effect of this configuration on total CPL measurements. In the ideal case, a non-overlap beam system would suffer little to no error in the CPL measurements assuming the system was imaging a target with constant reflectivity. In the experimental case, this is typically not true unless the DIAL system is configured to take static measurements where the reflector is a retroflector or other constant reflectance material a fixed distance away from the transmitter. To parallel the ANGEL system, we must consider that the airborne system will be using the ground return of the transmitted energy reflected back to the detector. Obviously, the terrain of the Earth does not have constant reflectance in the infrared, and as such, DIALSimV2 simulates the apparent increase or decrease in CPL as the systems' transmitted laser distribution is scanned across a region of varied reflectance. Because the two beams are not perfectly overlapped, the above parameter denoted as the scattering efficiency ρ^s cannot be held as a constant. The changes to the topographical scattering efficiency or reflectivity can be easily computed as follows,

$$\rho^s = \frac{\rho^s{}_1 A_{over} + \left(\rho_2{}^s \pi \left(\alpha R_T\right)^2 - A_{over}\right)}{\pi \left(\alpha R_T\right)^2} \qquad [14]$$

where,

$\rho_1{}^s$ is the scattering efficiency of one region [unitless],
$\rho_2{}^s$ is the scattering efficiency of the second region [unitless],
A_{over} is the area of the laser distribution subtended upon the first region [m^2] and,
α is the half angle divergence of the transmitting laser [radians].

The total reflectivity can be calculated in this manner assuming the laser distribution at range is Gaussian in nature. A laser not operating in TEM(0,0) would likely have a reflectance parameter far different from the theoretical value because of asymmetrical power distribution in the far field cross section.

The following set of figures show a simulation performed with arbitrary system parameters for a case of 100% overlap and then moving from a region of 10 to 1 percent reflectance. As shown by Figure 16(b), the measurement and reference reflectivity variation are the same because the beams are perfectly overlapping. The 3-D plot shown below in Figure 16(c) is a summation of the previous 'case 1' evaluated as the perfectly overlapped beams traverse the boundary. Consequently, as the boundary is crossed, there is no change for the expected measurement of plume size regardless of the size of plume being modeled.

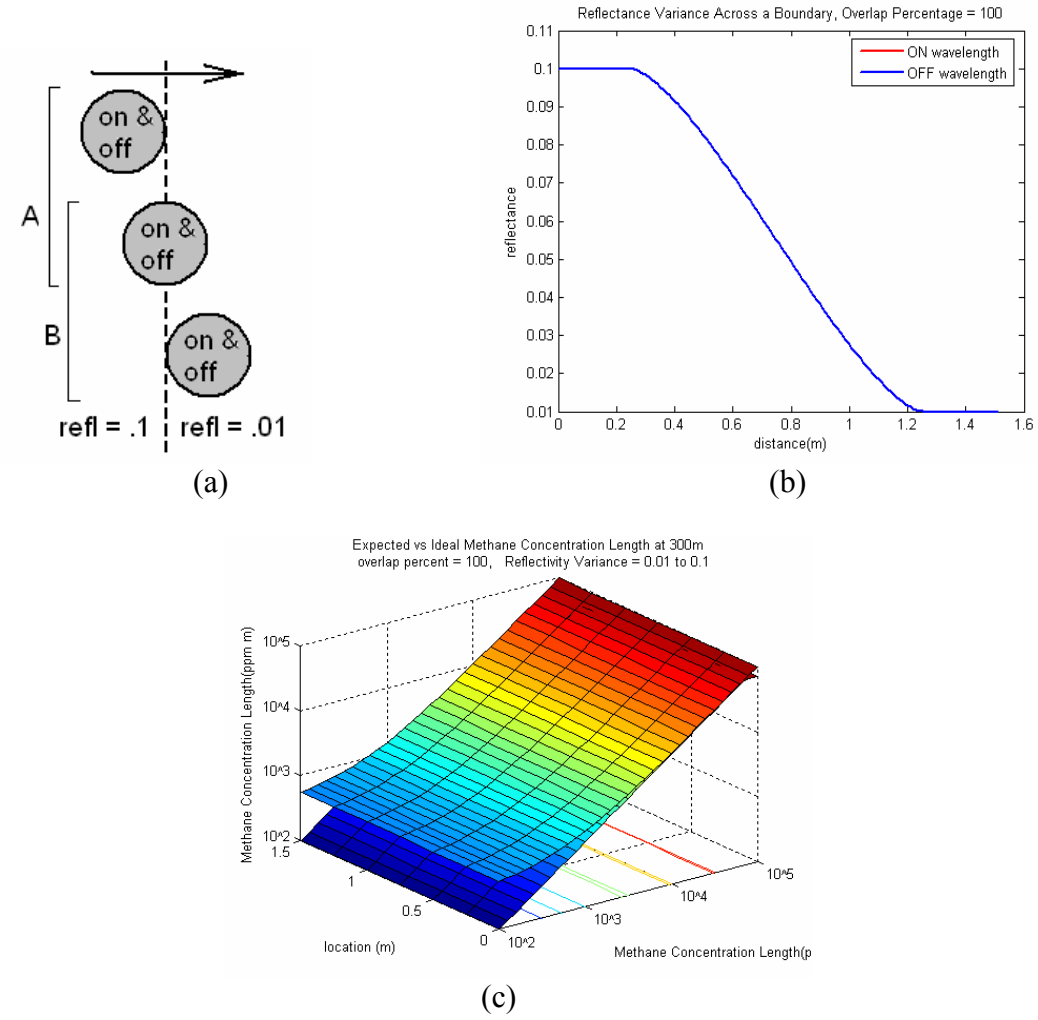

Figure 16: Results of 100% overlap simulation with selected input parameters.

Subsequent simulations were then performed for cases where there was a zero and partial overlapping of the measurement and reference beams at range with the measurement beam leading the reference beam to a region of lower reflectivity. Although a DIAL system operating with measurement and reference beams lacking well overlapping cross section at range causes severe error in CPL measurements, these test cases allow for the confirmation of the model findings. Figure 17 (a) and (b) respectively show the case setup and the fall of reflectivity for the

measurement wavelength prior to the reflectivity fall of the reference wavelength as the boundary is crossed.

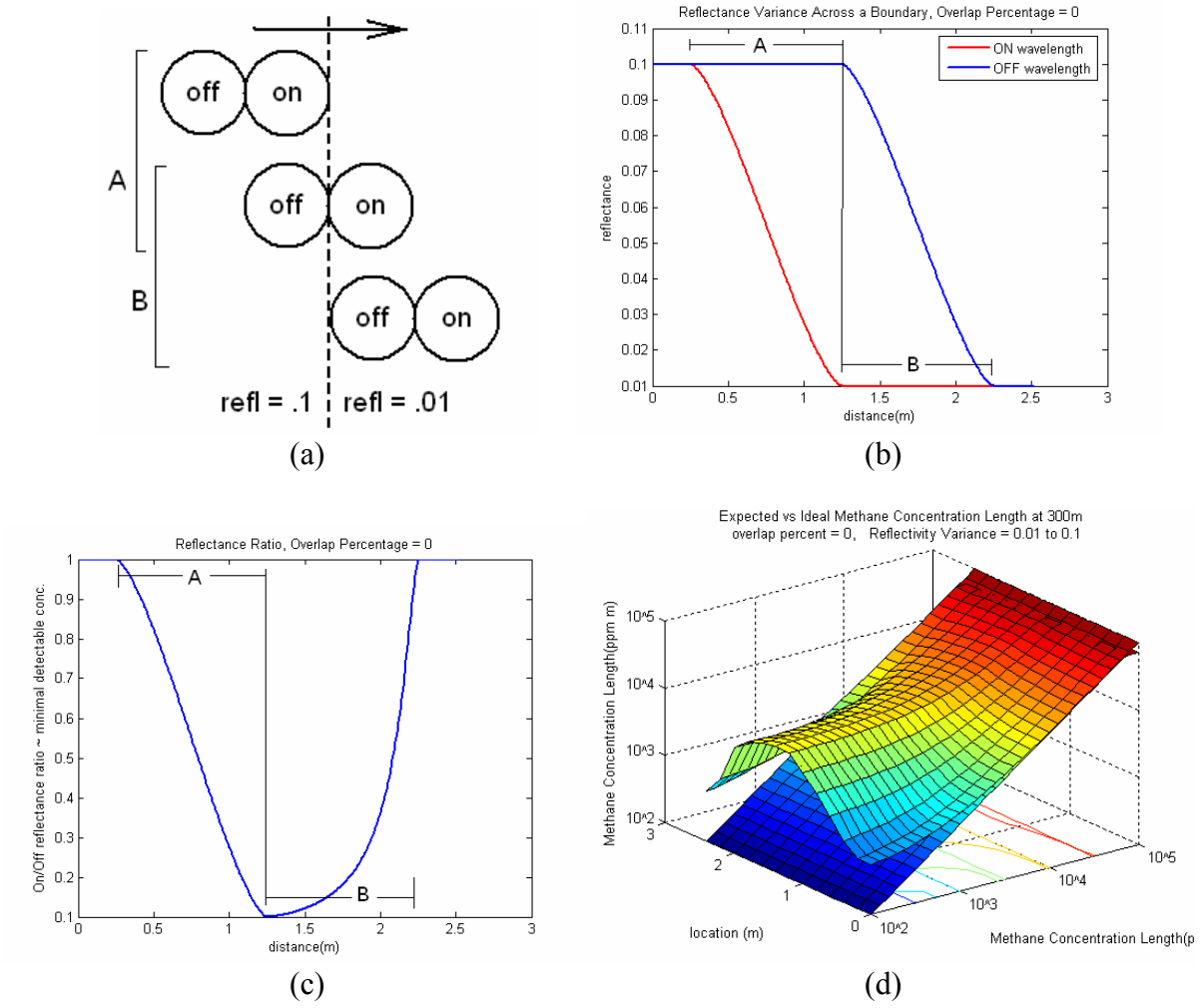

Figure 17: Simulation Results of 0% overlap, online leading.

The function of lower detectable limit can be divided into two sections labeled A and B, (Figure 17(c)) which can be visualized by the effect due to measurement beam traversing the boundary followed by the reference beam. These regions are not symmetrical because the different reflectivities create a weighting effect on each beam's total reflectance parameter as the area subtended upon each region is integrated. Further, it can be concluded through this simulation of

an arbitrary non-overlapping DIAL system that beam misalignment causes severe errors in CPL measurements when topographic reflectance parameters vary less than one order of magnitude.

The final Case 2 simulation was run for a system configured for a partially overlapping system at range over the same reflectivity variation as before, 10 to 1 percent. The results from this simulation are as shown below in Figure 18 (a) through (d).

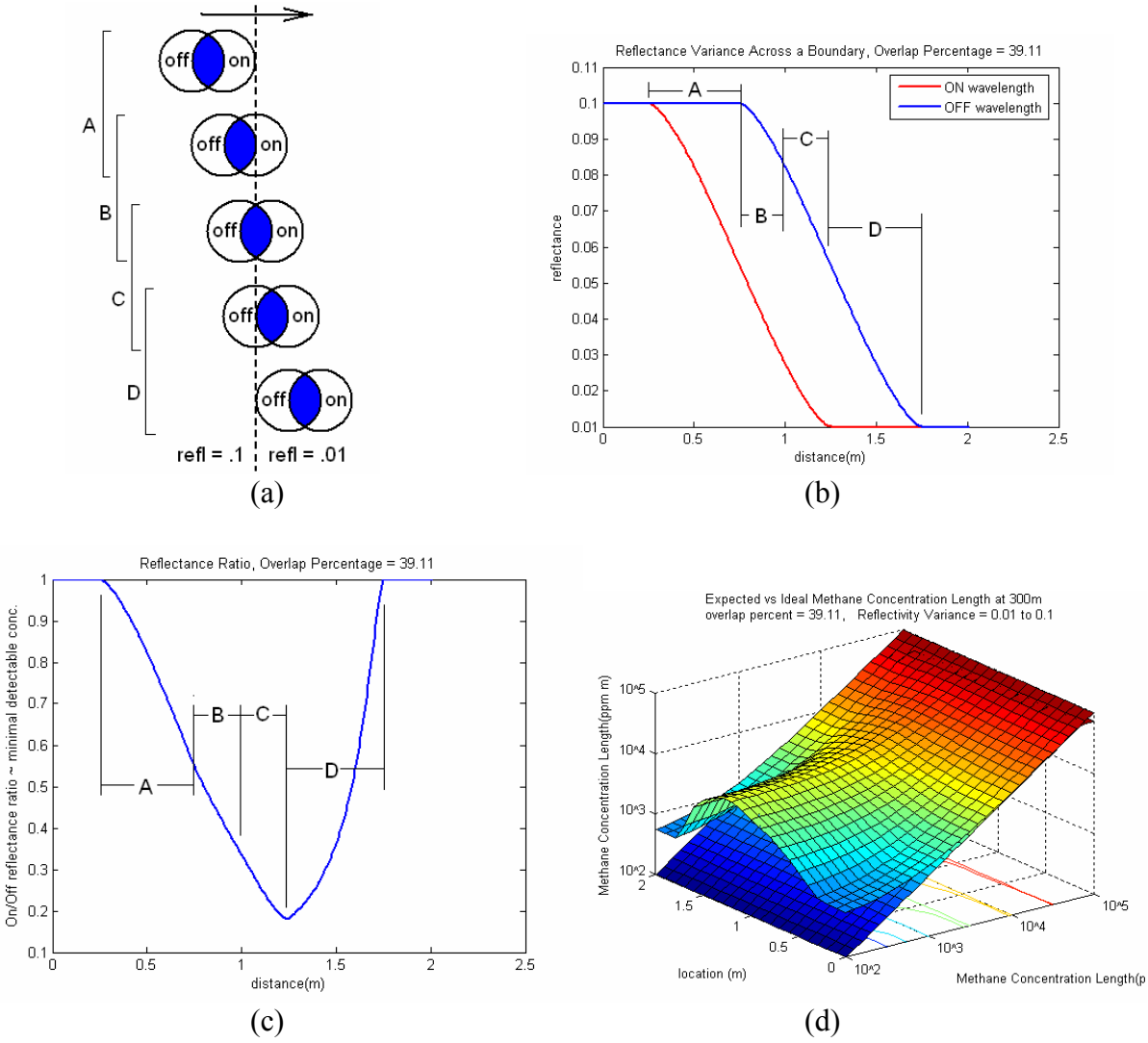

Figure 18: Results from simulation of partial overlap with online wavelength leading.

Notice that there are four distinct sections to the reflectance ratio plot shown as the lasers are scanned across the boundary of varied reflectance. As the far field pattern of the non overlapping beams is passed over the boundary, the anticipated increase in expected CPL reading occurs, although not as significant as the non overlapping case.

All three of the simulations discussed thus far were performed with the same measurement and reference wavelengths for methane in the 3-4 μm region of the spectrum. All system parameters were held constant except center-to-center distance of the far field distributions during each simulation. In addition, all were performed for cases where the measurement beam was leading the reference beam moving from a region of high to low reflectance. While examination of this most simple case is helpful, it is hardly useable for comparison to real world data. However, the latest version of DIALSimV2 allows for the user to choose the geometry of the transition. For example, in the event that measurement beam was trailing the reference beam moving from a high to a low reflectance an apparent decrease in expected CPL would be detected due to premature attenuation of the reference beam as shown in Figure 16(a). Figure 16(c) shows an additional option added to DIALSimV2 which allows the user to simulate the response of only 10^2, 10^3, 10^4, and 10^5 ppm·m concentration plumes to save on computing time.

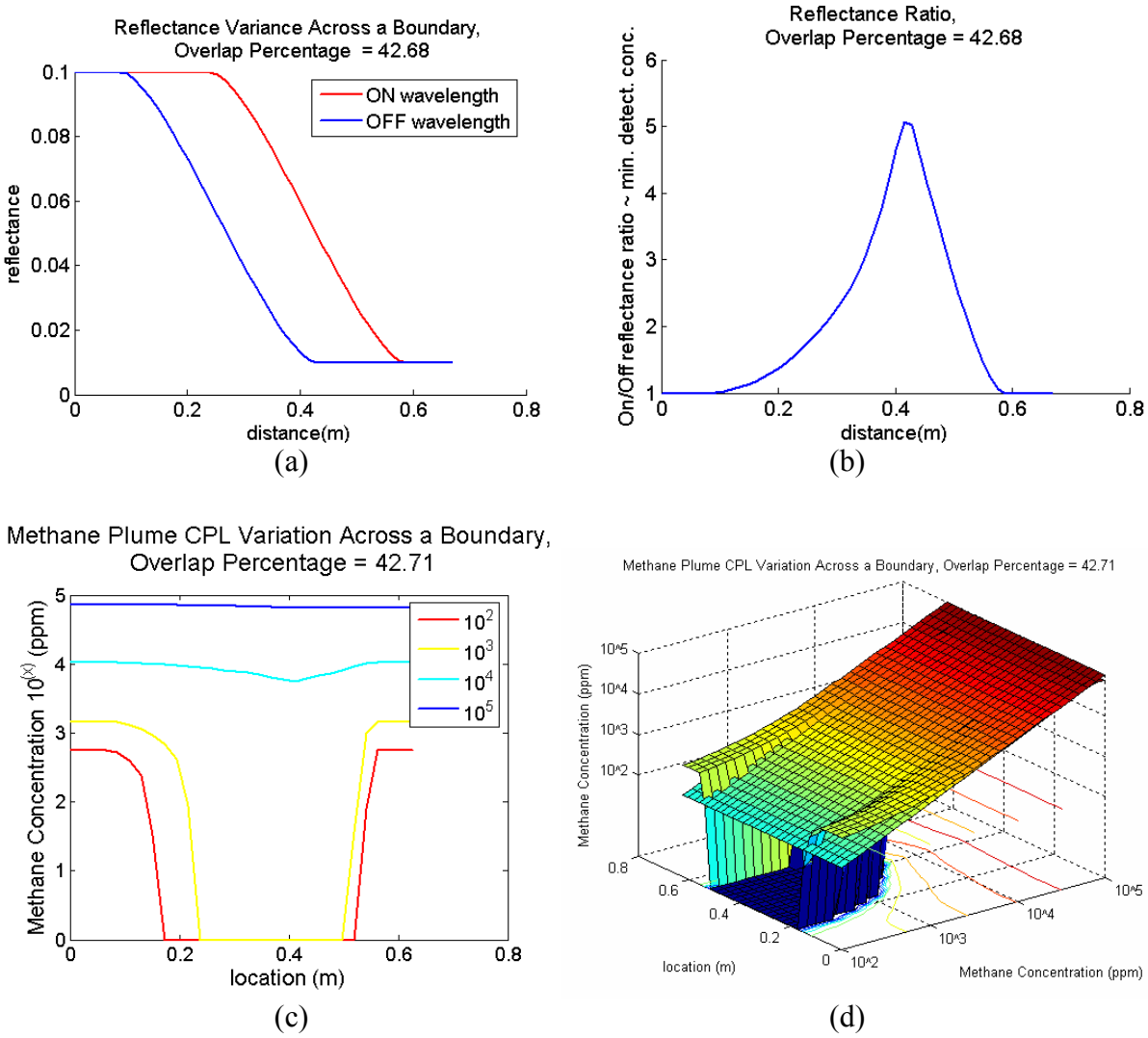

Figure 16: Results of partial overlap sim., offline leading, and arbitrary system inputs

'Case 3' of the DIALSimV2 allows for the calculation of the expected signature of a species of interest as a function of altitude for a given plume concentration. This calculation is highly dependent on the noise of the system and the background level of the species of interest. An example of this can be seen in the following simulation for methane. Assuming the noise in the system was negligible, background methane levels in the atmosphere corrupt the expected measured CPL of a given plume size as altitude is increased.

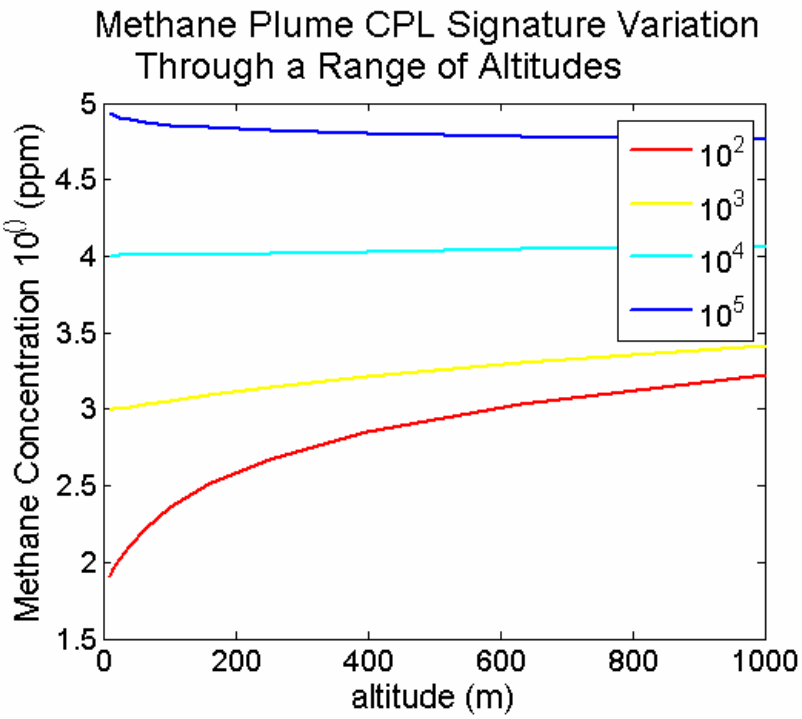

Figure 17: Methane minimum signature variation from 0 to 1km

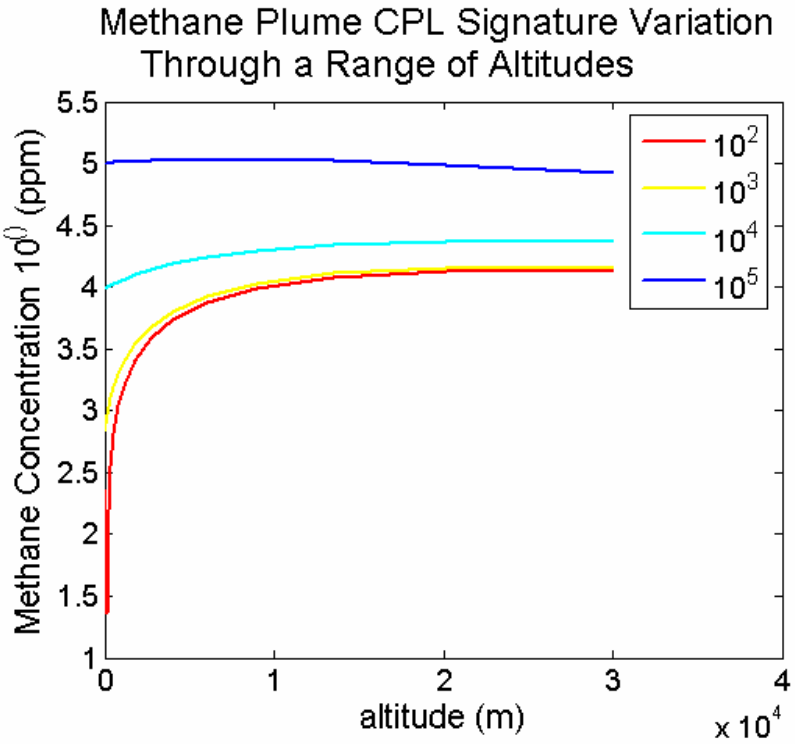

Figure 18: Methane minimum signature variation from 0 to 30km

Above 7-8 km the change in the lower detectable limit lessens due to the scale height of the atmosphere; however, as the physical size distribution of the measurement and reference beams increase due to a constant divergence, additional attenuation of the transmitted power occurs. Under best case scenario, this divergence would be diffraction limited, however even in this case, the effects of an increased volume of the propagation can still be observed. 'Case 3' of DIALSimV2 also has a 3D graphing option for all CPLs in between those shown above.

Comparison of DIAL LIDAR Simulation to ANGEL data

In an attempt to further verify the validity of the model, data from the ITT Industries ANGEL was acquired and used for a comparison. Initially the beam alignment of the online and offline lasers was known to be imperfect during integration and test. These speculations were further confirmed by an overlap test administered by Penn State Graduate students Joe Begnoche, Adam Willitsford and myself, using the Thermovision 400 Series camera. The same method of data acquisition described previously in this document (pgs. 16-19) was used to image both the online and offline beams in the field of view of the IR camera. A point of reference was chosen in the recordings to provide for the determination of size and center to center distance of the online-offline distribution from the processed IR camera movies. These overlap measurements provided the information necessary to estimate the methane CPL fluctuation during operation due to misaligned lasers traversing ground reflectivity variations. While the beam misalignment issue has since been repaired, the instrument data presented below was acquired shortly after the initial aircraft integration before the final beam alignment procedure. Therefore, the data contains ambiguities in the measured CPL information relative to the geometry of the collection instance. Although the amount of data acquired was limited, a simple example of a test flight over a runway at Buffalo Airport in New York State compared with some

of the findings of DIALSimV2 allowed for confirmation of the model. The following simulations assume that little to no change in the alignment occurred between the time the beams were imaged with the IR camera and the time of test flight. Therefore, the previously measured parameters for center to center distance and diameter were used in determining the following findings. Full release of ANGEL parameters entered into the PSU DIAL model is not possible at this time, therefore only relative fluctuation of methane CPL measurements follow. This is possible by presenting the following simulations and comparisons with axes scales removed.

The data set used for comparison was acquired when ANGEL flew down a runway between 300 and 1000 feet off the ground with the scanning unit off while imaging the tarmac on the 7th of October, 2004. At various times during the flight the far field distribution of the measurement and reference beams reflected off a periodic reflectors positioned in the middle of the runway. In addition, at the time of flight it was noted that the measurement and reference beams were slightly misaligned by an amount not available for release. In order to compare this real world flight data to the output of the DIALSimV2 model, the simulation was run for two slightly misaligned beams at the ANGEL system specifications. In addition to these input parameters, one additional change made to the PSU DIAL simulation, namely an addition to Case 2 where 3 different reflectivity regions could be modeled. In this case, target regions 1 and 3 were the same input, namely the chosen parameter for infrared tarmac reflectance. Target region 2 was adjusted to be a significantly higher reflectance simulating high reflective paint on the runway. The simulation was initially run for two cases being when the measurement beam was leading and the other when the reference beam was leading. Although not known at the time of flight, it was determined by a cursory scan of the flight data that the measurement beam was

leading as the far field distribution transitioned from the tarmac to the highly reflective paint. This case was then further reviewed with the DIALSimV2 results in Figure 19 (a) through (d).

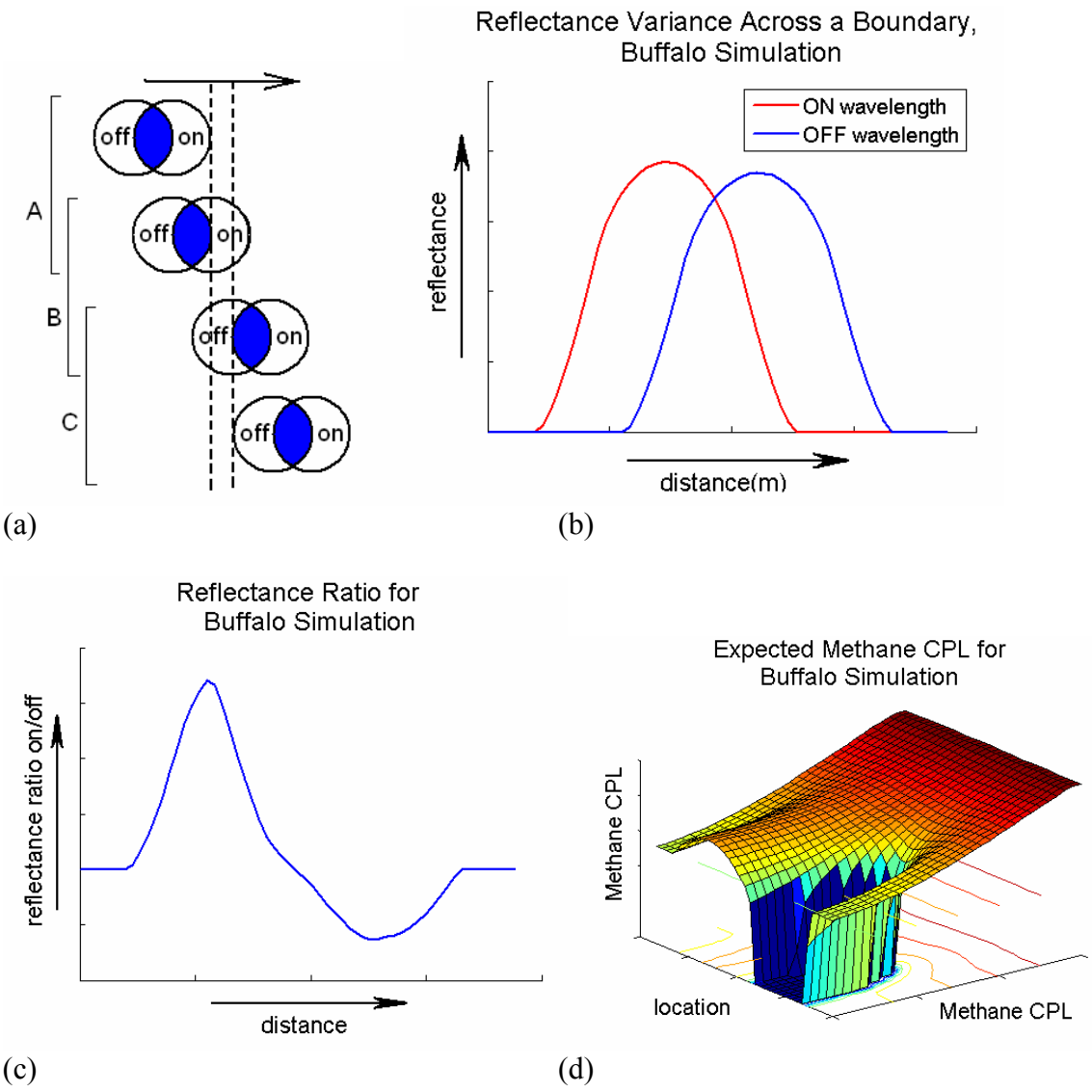

Figure 19: Simulation Results of the ANGEL System on Runway Flight 10/07/2005

As the leading measurement beam returns from the highly reflective paint, the on/off reflectance ratio climbs, as expected. This ratio subsequently falls and returns to the original value as the trailing reference beam moves across the highly reflective target region. The fluctuation in the on/off reflectance ratio causes a decrease and then subsequent increase in concentration path length across the distance of the scan, which can be observed by viewing the full simulation

result in part d. From this information it is speculated that the shape and magnitude of the CPL fluctuation depends on strength of the strong middle reflector, and the spatial distribution of the reflectivity variance relative to the beam size distribution at range.

To compare to the actual ANGEL data taken over the runway on October 7, 2004, we have chosen a section of simulation to extract. Knowing that there were no methane plumes being imaged at the time of data acquisition over the runway is the key in making the assumption that the lower detectable limit (LDL) of the simulated system must be used in the comparison. If the beams were perfectly aligned, this lower detectable limit of the system would obviously be flatlined at the CPL reading corresponding to the noise level present in the system. Misalignment in the ANGEL system caused periodic deviation from this ideal case as the beams struck the highly reflective paint on the runway as shown in Figure 20.

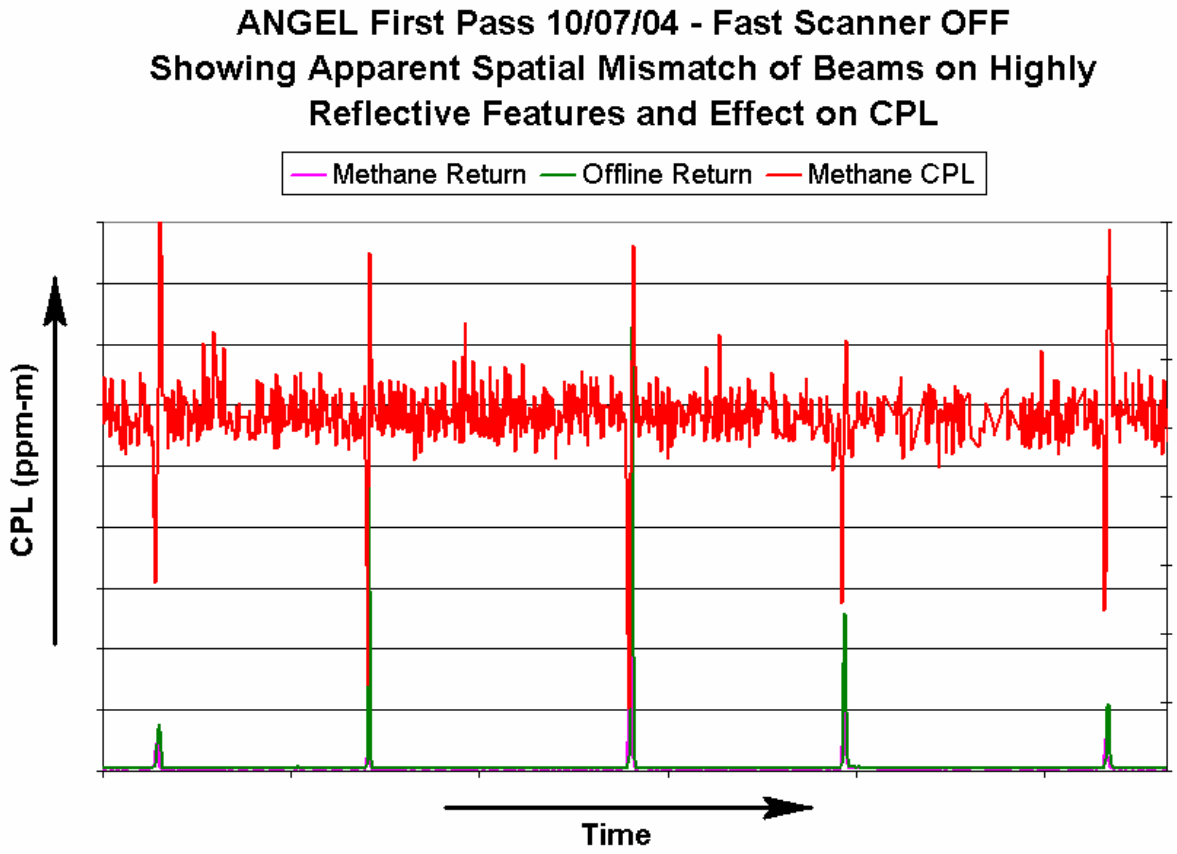

Figure 20: CPL fluctuation due to striking of reflective strips in runway.

When comparing the ANGEL data to the simulated data we must use the LDL fluctuation of the DIALSimV2 results as there were no plumes being imaged in the far field. This corresponds to the values described by the region of the 3D plot in the (CPL, CPL) plane where the slope of the graph begins to approach zero. Consequently, as plume size continues to decrease, the expected measured CPL will approach a constant value. This value is inherent due to background absorption of the species of interest or noise in the system, and hence describes the effective LDL of the system. Although a quantitative assessment of how these apparent CPL readings compare cannot be revealed, the relative CPL fluctuation for the actual and simulated cases are subsequently presented in Figure 21.

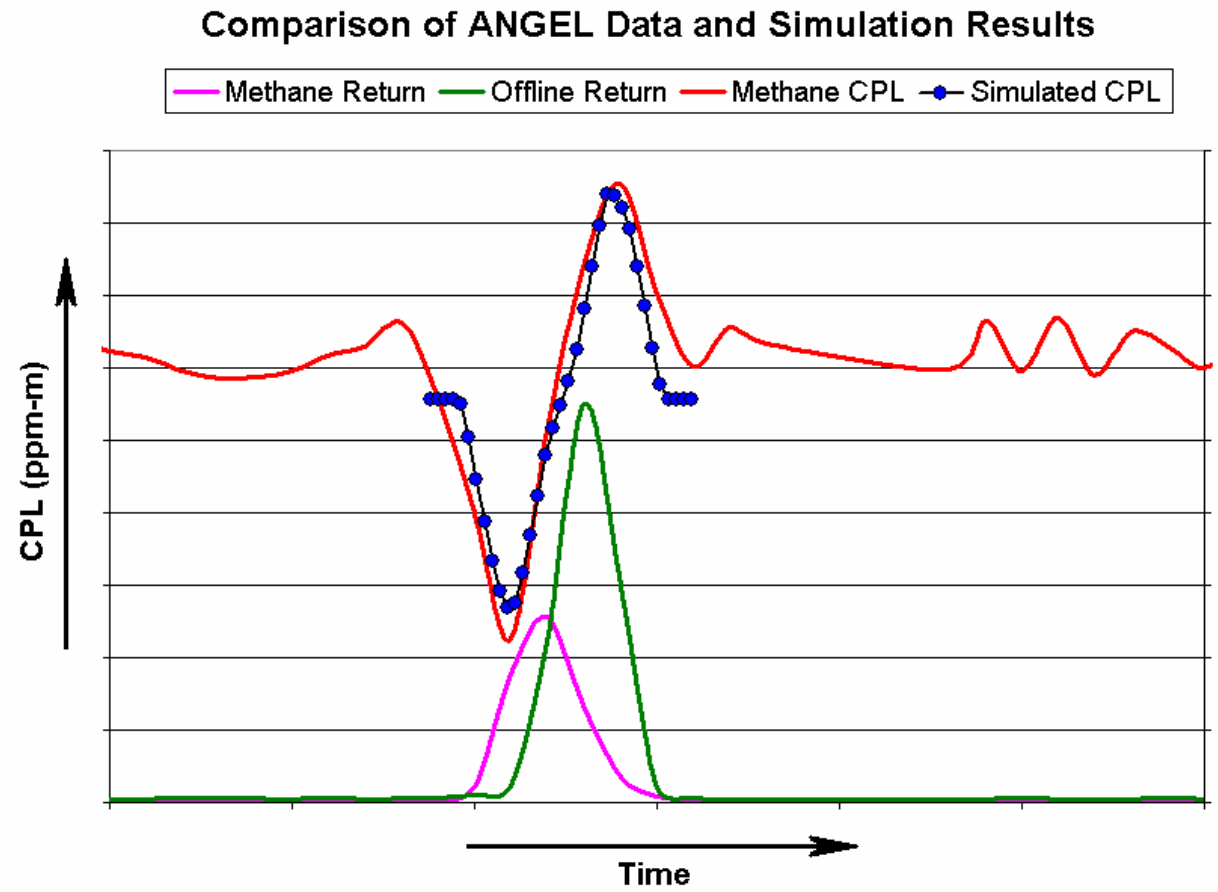

Figure 21: Simulated results as compared to actual ANGEL data.

As shown, the background noise CPL level for the simulation appears to be less than the background noise of the actual data, assuming the constant regions across time are averaged. This effect is likely due to DIALSimV2 using estimated ANGEL system noise parameters for both sides of the transceiver as actual noise values are currently not available for release. A second possible reason for deviation from the simulated response would be the effect of the beam distribution not moving normal to the reflectivity boundary or incorrect size of the highly reflective strip on the runway.

Conclusions

It has been shown by this study that remote sensing techniques in the midwave infrared region of the electromagnetic spectrum are possible and robust due to the low background earth radiance in the region. Infrared source theory and examples were able to demonstrate that the equipment necessary to create the transmitting side of an active remote sensing instrument in this region of the spectrum exist. In addition, various types of detectors were broadly reviewed with a specific description of how the Thermovision series 400 Camera operates, and how it was used to measure a pulsed infrared source in 3-4 um region. Using the accumulated knowledge of emitters and detectors, the reader was presented with the high level design basics of a DIAL lidar system together with an equivalent model of such a system. The results of various arbitrary simulations performed with DIALSimV2 were presented in an attempt to explain effects of imperfect beam overlap on DIAL lidar performance. Numerous example simulations were performed and reasoned as to confirm the validity of the model. Lastly, simulation results were compared to measured data from the DIAL lidar used in the ITT Space Systems Inc. ANGEL service. A striking correlation between the simulated and measured results was found, and the small ambiguities are most likely due to the lack of all ANGEL system parameters. With the model findings validated, DIALSimV2 can be subsequently used for troubleshooting or general ANGEL system performance calculations. Additional ANGEL data would allow for further tailoring of DIALSimV2 to more effectively model performance and noise characteristics of the system.

References

Atkins, Peter W. Physical Chemistry, 4th Edition. W.H. Freeman and Company, New York, 1990.

Electro Optical Industries Inc. "Education and Reference of Detectors" 2000. http://www.electro-optical.com

Grund, Christian J.; Shald, Scott; Stearns, Steven V. "Airborne three-line mid-IR DIAL for rapid chemical species plume mapping" *Proceedings of the SPIE*, Volume 5412, September 2004, pp1-9.

Li, Guangkun. "Atmosphereic Aerosols and Particle Properties Using Lidar" Ph.D. Dissertation The Pennsylvania State University. 2004

Measures, Raymond M., Laser Remote Sensing.Wiley-Interscience, New York, 1984.

Philbrick, C. R. "Remote Sensing of Atmospheric Properties using Lidar" . Penn State University, University Park, PA 16802. ISSR 2003

Stearns, Steven V. "Airborne Assessment of Pipeline Integrity" *GeoIntelligence.* March/April 2005

Stearns, Steven V.; Lines, Raymond T.; Grund, Christrian J.; Philbrick, Russell C. "Active Remote Detection of Natural Gas Pipeline Leaks" U.S. Department of Energy National Energy Technology Laboratory Technology Status Report. 2004

Thermovision 400 Series Operating Manual. Agema Infrared Systems. Danderyd, Sweden.

Walmsley, Harold L.; O'Connor, Simon J. "The accuracy and sensitivity of infrared differential absorption lidar measurements of hydrocarbon emissions from process units." *Pure Appl. Opt.* **7** (1998) 907–925.

Wolfe W. L., Introduction to Infrared System Design - Tutorial Texts in Optical Engineering Vol. TT24', SPIE, 1996.